Bachelor's thesis

NTNU
Norwegian University of Science and Technology
Faculty of Natural Sciences
Department of Materials Science and Engineering

Magnus Breimo
Odin Vassbotn Breivik

Using Rotating Permanent Magnets for Pumping Aluminium in a Liquid Metal Loop

Bachelor's thesis in Materials Science & Engineering
Supervisor: Robert Fritzsch
Co-supervisor: Paul Bosworth, Joseph Whitworth
May 2024

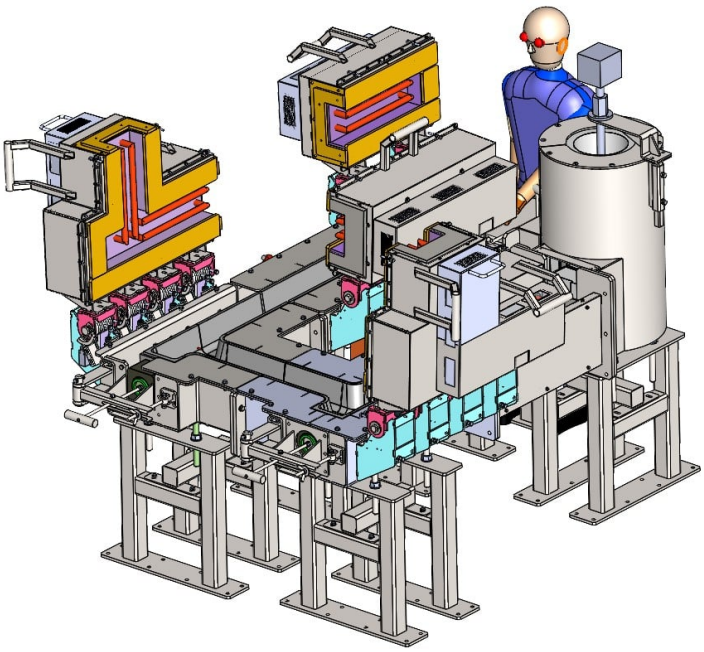

Supplied by Robert Fritzsch

NTNU
Norwegian University of Science and Technology

Pyrotek

Magnus Breimo
Odin Vassbotn Breivik

Using Rotating Permanent Magnets for Pumping Aluminium in a Liquid Metal Loop

Bachelor's thesis in Materials Science & Engineering
Supervisor: Robert Fritzsch
Co-supervisor: Paul Bosworth, Joseph Whitworth
May 2024

Norwegian University of Science and Technology
Faculty of Natural Sciences
Department of Materials Science and Engineering

NTNU
Norwegian University of
Science and Technology

NTNU
Kunnskap for en bedre verden

Department of Materials Science and Engineering

TMAK3001 - Bachelor Thesis Materials Technology

Using Rotating Permanent Magnets for Pumping Aluminium in a Liquid Metal Loop

Bruk av roterende permanente magneter for pumping av aluminium i en løkke med flytende metall

Authors:
Magnus Breimo, Odin Vassbotn Breivik

Supervisor:
Robert Fritzsch

External Supervisors:
Paul Bosworth, Joseph Whitworth

Project number:
IMA-B-20-2024

Spring, 2024

Abstract

The aluminium industry is dependent on pumping liquid metal during recycling processes. Due to the high corrosive characteristics of liquid aluminium, the existing methods for pumping need to avoid contact between the pumping equipment and the aluminium itself. This is done mainly by using electromagnetic stirrers and pumps, as a substitute for conventional mechanical pumping, which are still used in today's industry.

Investigating the possibilities of using permanent magnets instead has been a topic for debate, but few have used actual liquid aluminium in equipment that resembles industrial grade for academic investigation. Observing the market shows a few commercial vendors offering permanent magnetic solutions for pumping and even for stirring, but they are a side occurrence up to today.

This thesis investigates this possibility using a combination of solid and liquid aluminium trails in a custom setup working towards implementing the design of a permanent magnetic pump in a Liquid Metal Loop for semi-industrial academic research. Additionally, a finite element modelling (FEM) simulation of the system, using Comsol Multiphysics®, is made to compare the theoretical and the experimental approach to this problem. Using a permanent magnet (NdFeB type) with an inner magnetization of 1.45T, rotating it at a defined speed and distance, 37N of directional thrust force on solid aluminium billets was achieved. The force largely depends on the conductivity of the aluminium and the distance from the magnet to the aluminium. It was possible to create motion on the surface of a liquid aluminium bath, where the magnet was held below the melt.

Furthermore, the FEM simulation was sufficiently accurate to verify the findings about the size of the interaction volume of the magnetic field in the aluminium. This points towards the feasibility of using rotating permanent magnets to stir liquid aluminium on a full industrial scale.

Sammendrag

Aluminiumindustrien er avhengig av å pumpe flytende metall under resirkuleringsprosesser. På grunn av de høye korrosive egenskapene til flytende aluminium, må de eksisterende metodene for pumping unngå kontakt mellom pumpeutstyr og aluminium. Dette gjøres hovedsakelig ved bruk av elektromagnetiske rørere og pumper som en erstatning for konvensjonell mekanisk pumping, som fortsatt brukes i dagens industri.
Å undersøke mulighetene for å bruke permanente magneter i stedet har vært et tema for debatt, men få har brukt faktisk flytende aluminium i utstyr som ligner industristandard for akademisk undersøkelse. En observasjon av markedet viser noen få kommersielle leverandører som tilbyr permanente magnetløsninger for pumping, men de har hittil vært en sidesak.
Avhandlingen undersøker denne muligheten ved å utføre forsøk på fast og flytende aluminium i en spesialtilpasset oppstilling som arbeider mot implementering av designet til en permanent magnetpumpe i en løkke med flytende metal for semi-industriell akademisk forskning. I tillegg lages en FEM simulering av systemet, ved bruk av Comsol Multiphysics®, utført for å sammenligne den teoretiske og den eksperimentelle tilnærmingen til dette problemet. Ved å bruke en permanent magnet (NdFeB type) med en indre magnetisering på 1.45T, roterende med en definert hastighet og avstand, var det mulig å oppnå toppkrefter på 37N retningsbestemt skyvekraft på solid aluminium. Kraften avhenger i stor grad av ledningsevnen til aluminiumet og avstanden fra magneten til aluminiumet. Det var mulig å skape bevegelse på overflaten av et flytende aluminiumsbad, hvor magneten ble holdt under smelten.
Videre var FEM-simuleringen tilstrekkelig nøyaktig til å bekrefte funnene om størrelsen på interaksjonsvolumet til magnetfeltet i aluminiumet. Dette peker mot muligheten for å bruke roterende permanente magneter til å røre flytende aluminium i full industriskala.

Preface

This project was made possible by the Norwegian University of Science and Technology (NTNU) and Pyrotek. The group decided to obtain this specific assignment due to the interesting experimental and theoretical work connected to the task. The assignment itself was supplied by the Department of Materials Science and Engineering, IMA, NTNU. Firstly, we would like to thank our supervisor, Robert Fritzsch, who has overseen and contributed greatly to all aspects of the project work. This project would not have been possible without him. Secondly, our external supervisors, Paul Bosworth and Joe Whitworth from Pyrotek, have helped us during the initial work, by sharing years of experience in the industry helping us understand how engineers work to solve tasks. We would also like to thank Toms Beinerts from the Institute of Physics at the University of Latvia for supporting our work with the FEM model used in this project. While working on the experimental trials, Amund Ugelstad, who spent most of his spare time in the workshop, helped us when we struggled to find good solutions. Also, he machined many parts that were important for the experimental trials. We would like to thank Hannes Zedel for reviewing and commenting on our writing, and how to present the content. Lastly, we would like to thank our comrades, Ole Stensby and Magnus Odland, for sharing the office, and mental support during the semester.

Statutory Declaration

We declare that we have developed and written the enclosed thesis entirely by ourselves and in collaboration with the group signed onto this work, and have not used sources or means without declaration in the text. Any thoughts or quotations, which were inferred from these sources, are clearly marked as such.

This report was not submitted in the same or in a substantially similar version, not even partially, to any other authority to achieve an academic grading and was not published elsewhere.

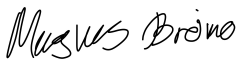

Magnus Breimo	20.05.2024, Trondheim
	Date

Odin Vassbotn Breivik	18.05.2024, Trondheim
	Date

Contents

Contents v

List of Figures vii

List of Tables viii

Abbreviation ix

List of symbols x

1 Introduction 1

2 Theory 2
2.1 Aluminium and its properties . . . 2
2.1.1 Electrical conductivity . . . 2
2.1.2 Thermal conductivity . . . 3
2.2 Permanent magnet . . . 4
2.3 Magnetic field theory . . . 4
2.3.1 Fundamentals of AC motors . . . 6
2.3.2 Rotating permanent magnet . . . 8
2.3.3 Lorentz forces . . . 8
2.3.4 Gaussmeter . . . 8
2.3.5 Penetration depth . . . 10
2.4 Pumping of liquid aluminium, the premise of magnetohydrodynamics . . . 10
2.5 Induction Heating . . . 11

3 Experimental approach 12
3.1 Materials and Equipment . . . 12
3.2 Measurement of Magnetic Field . . . 13
3.3 Building Test rig for PMP . . . 14
3.3.1 First iteration . . . 15
3.3.2 Second Iteration . . . 17
3.3.3 Third Iteration . . . 17
3.4 Test approach for PMP test rig . . . 18
3.4.1 Test of thermal effect . . . 19
3.4.2 The thrust test . . . 20
3.4.3 Validation with liquid aluminium . . . 21
3.5 LML . . . 21

4 Results and Discussion 23
4.1 Sources of Error . . . 23
4.1.1 Measurement of Magnetic flux . . . 24
4.1.2 Measurement of Thrust . . . 24
4.1.3 Measurement of Thermal effect . . . 24
4.1.4 Validation with Liquid Aluminium . . . 24
4.1.5 Plotting and data . . . 24
4.2 Magnetic Flux Density . . . 24
4.3 Results from test rig . . . 26
4.3.1 Thrust . . . 27
4.3.2 Thermal effect . . . 30
4.3.3 Comsol Multiphysics® . . . 32
4.4 Validation with liquid aluminium . . . 37

5 Conclusion 38

6 Future Work 39

References 40

A Risk assessment xi

B Gear change calculations xii

C Thrust graphs xiii

D Derivation of penetration depth xv

E Modelling from COMSOL Multiphysics® 5.5 xvi

List of Figures

1 Flow chart showing the planned content of the project. . . . 1
2 Flow chart describing the content for the theoretical section. . . . 2
3 Electrical resistivity of pure aluminium and alloys [16]. . . . 3
4 Magnetic flux travelling from the north pole (N) to the south pole (S) [24]. . . . 5
5 Hysteresis curve of a hard and soft magnet from [21] page 380. . . . 6
6 Principals for AC magnetic field in a motor [12]. . . . 7
7 Lorentz force illustrated by the right-hand rule. . . . 8
8 The Hall Effect demonstrated. A current is going through the specimen in the x-direction while a magnetic field is imposed in the z-direction resulting in a deflection of the charge carriers in the y-direction, found on page 70 in Callister et al. [24]. . . . 9
9 Common probe types for Gaussmeters [8] figure 5 page 3. . . . 9
10 Flow chart describing the content for the experimental approach. . . . 12
11 Rudimentary sketch of magnet and measurement points. . . . 13
12 Digitized measuring points based on Figure 11. . . . 13
13 Gaussmeter-probe held in place with Styrofoam. Position controlled with vernier. . . . 13
14 Magnet inserted in Styrofoam. Sides 1 and 2 were measured. . . . 13
15 The testing setup for the magnetic field visualization using iron filings. . . . 14
16 Front facing model for visualizing magnetic field with iron filings. . . . 14
17 Rudimentary sketch of the first idea for the test rig. . . . 15
18 Model of test rig constructed from aluminium frames. . . . 16
19 Measuring the cuts from a template piece. . . . 16
20 Cutting the aluminium profiles. . . . 16
21 Rig without motor or magnet support. . . . 17
22 The completed first iteration of the rig. . . . 17
23 Overview of the third iteration of the rig. (a) is the position of the Load cell, (b) is the rotating permanent magnet, (c) is the FLUKE® multimeter, and (d) is the Aluminium billet (6082). The multimeter was connected to a computer for continuous data logging. 18
24 Gear system of the third iteration of the rig. Consisting of the motor and the five-tier pulleys with a fan belt connection. . . . 18
25 RPM of the motor as a function of input Hz in the inverter. . . . 18
26 Five-tier pulley system with numbers indicating gears. . . . 19
27 Induction test on Aluminium billet. The figure gives an overview of the setup. The test consists of (a) two k-type thermocouples, a (b) Load cell, a (c) rotating magnet, a (d) water inlet and an (f) outlet, a (e) Temperature logger, a Scale to measure the flow of water underneath the outlet, and a (g) PC for logging data from the load cell, water flow and temperature simultaneously. . . . 20
28 Model of the relative position of the thermal effect test, where the magnet was 0.5cm above the billet. . . . 20
29 Model of the relative position of the thermal effect test, where the magnet was 2.0cm above the billet. . . . 20
30 Setup for the preliminary liquid metal trials. . . . 21
31 Visual setup of verification trial. . . . 21
32 CAD of LML . . . 22
33 Overview of LML with one open lid and one closed. . . . 22
34 LML with open lids revealing the refractory lane, and the heat elements in the lids. . . . 22
35 Flow chart describing the content for results and discussion. . . . 23
36 The magnetic field as a function of distance from the magnet. Measured from the middle of the length of the magnet (5.5cm) on side 1. . . . 26
37 Magnetic field shown with iron filings from the ”strong” side of the magnet, side 1. . . . 26
38 Magnetic field shown with iron filings from the ”weak” side of the magnet, side 2. . . . 26
39 Plots of the force as a function of frequency at 0.5cm above the billet. . . . 27
40 Thrust on the load cell as a function of frequency at different heights above the billet. . . . 28
41 Plot of the penetration depth as a function of frequency. The black dotted lines indicate the maximum and minimum frequency measured in the thrust test. . . . 28

42 Force as a function of distance into the billet at 50Hz and with the magnet 0.5cm above the billet. Calculated using Equation 12. Different penetration depths (δ) are shown to the end of the billet, at 5cm. . . . 29
43 Penetration depth and Force readings plotted in the same figure, sharing the x-axis. . . . 29
44 Penetration depth and the inverse of the force readings plotted in the same figure with a shared x-axis. . . . 30
45 Temperature as a function of time for both tests, as well as the difference between temperature in - and temperature out of the billet. In the graph, only temperature out is shown and the heating up and cooling down regions are removed. . . . 31
46 Heat loss expressed as watt as a function of time. As well as the average heat loss for the whole test. Test 1 was conducted 0.5cm above the billet, and test 2 was conducted 2.0cm. The graphs are edited to show only the results gathered from the equilibrium state of the system. Meaning the results from the heating up and cooling down of the billet are removed. . . . 31
47 Force as a function of time throughout the thermal test experiment. . . . 32
48 Comsol Multiphysics® model of the magnet and the billet used in the Finite element modelling (FEM) simulation. . . . 32
49 3D model of the system showing the billet from the front. . . . 33
50 3D model of the system from the side, showing the flux line distribution in the billet clearly. . . . 33
51 The penetration of the magnetic field lines through the billet seen from the front of the billet. . . . 34
52 The penetration of the magnetic field lines through the billet seen from the side. . . . 34
53 Liquid aluminium before validation test. . . . 37
54 Liquid aluminium during validation test. . . . 37

List of Tables

1 List of Abbreviations . . . ix
2 List of Symbols . . . x
3 Designation for Aluminium alloys [3]. . . . 2
4 Properties and grades of NdFeB magnets [20]. . . . 4
5 Properties and grades of SmCo magnets [20]. . . . 4
6 Description of AC-motor theory based on Figure 6 by The U.S. Department of Energy [12]. . . . 7
7 Gear settings used in the experiments with the corresponding diameters of the gear-wheels. . . . 19
8 Magnetic flux, DC, side 1 of magnet. . . . 25
9 Magnetic flux, DC, side 2 of magnet. . . . 25
10 Parameters of the thermal test. . . . 30
11 COMSOL Multiphysics® induction loss modelling simulation, 0.5cm above billet (6060). 35
12 COMSOL Multiphysics® induction loss modelling simulation, 2.0cm above billet (6060). 36
13 COMSOL Multiphysics® induction loss modelling simulation, 1.0cm above billet (6060) xvi

Abbreviations

Table 1: List of Abbreviations

Abbreviation	Definition
AC	Alternating Current
DC	Direct Current
LML	Liquid Metal Loop
MHD	Magnetohydrodynamics
PMP	Permanent Magnet Pump
EMP	Electromagnetic Pump
EMS	Electromagnetic Stirring
CAD	Computer-Aided Design
NTNU	Norwegian University of Science and Technology
RPM	Revolutions Per Minute
3D	Three-Dimensional
2D	Two-Dimensional
FEM	Finite Element Modelling

List of symbols

Table 2: List of Symbols

Symbols	Meaning	Units
σ	Electrical Conductivity	$[\frac{S}{m}]$
ρ	Resistivity	$[\Omega \cdot m]$
ρ_{total}	Total resistivity	$[\Omega \cdot m]$
ρ_{t}	Temperature contribution on resistivity	$[\Omega \cdot m]$
ρ_{i}	Impurity contribution on resistivity	$[\Omega \cdot m]$
ρ_{d}	Deformation resistivity	$[\Omega \cdot m]$
B	Magnetic flux density	$[T]$
M	Magnetization	$[\frac{A}{m}]$
H	Magnetic field strength	$[\frac{A}{m}]$
μ	Permeability	$[\frac{H}{m}]$
μ_0	Permeability of free space	$[\frac{H}{m}]$
μ_r	Relative permeability	[-]
$\vec{F}$	Lorentz force	[N]
$\vec{J}$	Current density	$[\frac{A}{m^2}]$
$\vec{E}$	Electric current density	$[\frac{V}{m}]$
$\vec{B}$	Magnetic flux	[T]
V_H	Hall voltage	[V]
I_x	Current	[A]
R_H	Hall coefficient	$[\frac{m^3}{As}]$
B_z	Magnetic field	[T]
d	Thickness of specimen	[m]
δ_c	Penetration depth	[m]
α	Attenuation constant	$[\frac{1}{m}]$
l	Distance travelled in lossy medium	[m]
f	Frequency	[Hz]
$q_{calorie}$	Calorimetric energy	[J]
C_s	Specific heat capacity	$[\frac{J}{kg \cdot K}]$
ΔT	Temperature change	[K]
Q	Effect	[W]
$\dot{m}$	Mass flow	$[\frac{kg}{s}]$
$C_{s,w}$	Specific heat capacity of water	$[\frac{J}{kg \cdot K}]$

1 Introduction

In the aluminium industry, scrap recycling is becoming increasingly important as the aluminium electrolysis process is very energy-consuming and demanding on the environment. The main challenge for recycling aluminium is managing impurities introduced from all the different alloys that are melted down. During the recycling and remelting of aluminium, the required energy can be reduced by appropriate mixing of the melting furnace. This is ideally achieved by forced agitation and here by a contact-free pump or stirrer. Electromagnetic pumps are commercially used for these applications as they do not contaminate the melt with physical contact of the impeller with the melt and also provide an extraordinary lifetime due to contact-free operation. This thesis work is here investigating the application of permanent magnetic agitation as an alternative to electromagnetic systems. The system will be installed into a semi-industrial scale liquid metal loop (LML).

To investigate the performance and properties of the magnet, and a permanent magnetic pump (PMP), we used a Gaussmeter and iron filings to map the magnetic field. Furthermore, thrust and induction heat loss was measured with two different test setups. Theoretical thrust and induction heat loss were calculated using finite element modelling (FEM) in COMSOL Multiphysics® 5.5. The results were compared, discussed and in the end evaluated. An overview of the planned work for the project is shown in Figure 1. Because the project consists of experimental trials, a risk assessment is included in Appendix A.

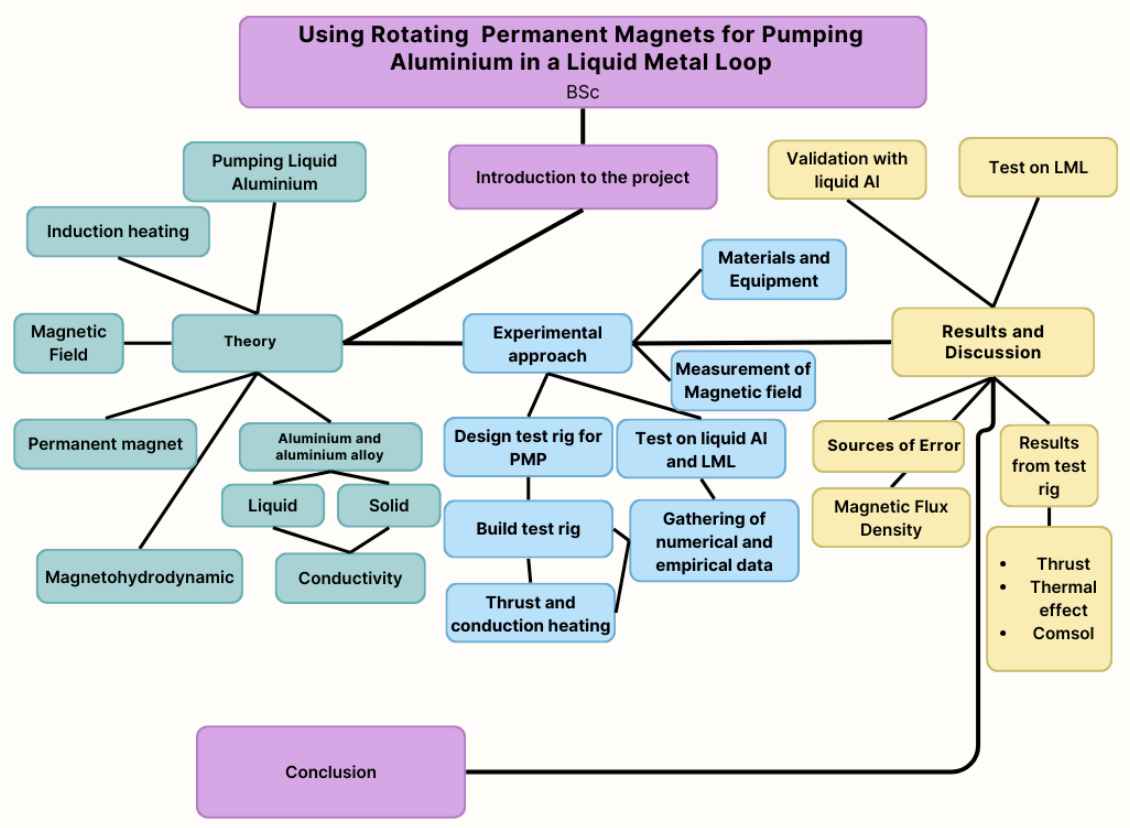

Figure 1: Flow chart showing the planned content of the project.

2 Theory

This project sets out to use rotating permanent magnets to pump liquid aluminium in a LML. Understanding the fundamentals of aluminium, conductivity, permanent magnets, magnetic field, pumping aluminium and induction heating is considered necessary knowledge to set forward. In Figure 2, an overview of the theoretical section is shown.

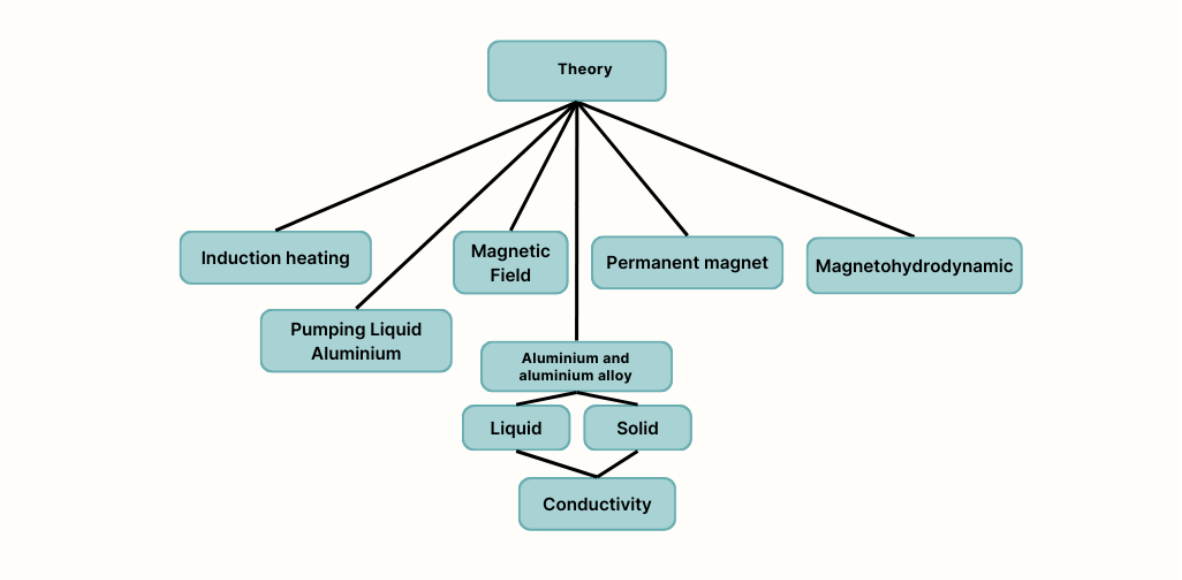

Figure 2: Flow chart describing the content for the theoretical section.

2.1 Aluminium and its properties

Aluminium is a metal that has seen industrial-scale production for less than 150 years, yet it is one of the most important engineering materials today. This is because of its many beneficial mechanical and physical properties. These include superior thermal and electrical conductivity, low density, and good ductility [19, 10, 18]. Designation for the commercial standard aluminium alloys is shown in Table 3 and refers to a 4-digit number, where the first digit denotes the major alloying element.

Table 3: Designation for Aluminium alloys [3].

Series	Alloy element
1xxx	99% aluminium, Al
2xxx	Copper, Cu
3xxx	Manganese, Mn
4xxx	Silicon, Si
5xxx	Magnesium, Mg
6xxx	Magnesium-Silicon, Mg-Si
7xxx	Zinc, Zn
8xxx	Other

2.1.1 Electrical conductivity

Aluminium is one of the most electrically conductive elements in use today. The electrical conductivity of pure aluminium results from the high electron mobility and number of free electrons present in its lattice. This allows electrons to move easily under the effect of even a weak electric field. The resistivity of a material can be described as the inverse of the conductivity, shown in Equation 1. Whereas in SI units, ρ is the resistivity $[\Omega m]$, and σ is electrical conductivity $[\frac{S}{m}]$ [24, 21]. However, electrical conductivity is also measured by; International Annealed Copper Standard (IACS) [13].

This is a standardized value based on annealed copper, from which every material can be assigned a percentage value of its conductivity.

$$\sigma = \frac{1}{\rho} \tag{1}$$

For alloys, the resistivity depends strongly on the type and amount of alloying elements. Matthiessen's rule describes this in Equation 2, which states that the electrical resistivity of any dilute alloy increases almost linearly with the amount of alloying elements added to the solution [24, 21, 14].

$$\rho_{total} = \rho_t + \rho_i + \rho_d \tag{2}$$

Where ρ_t is the contribution from temperature, ρ_d is the deformation resistivity, and ρ_i is the impurity contribution. The impurity and temperature contributions are the most significant regarding aluminium and its alloys. [24, 14]

2.1.2 Thermal conductivity

Thermal conductivity is a property that describes a material's ability to transmit heat [24]. As the thermal conductivity of a material is proportional to its electrical conductivity, aluminium will also have good thermal conduction. This relationship is described by the Wiedemann-Franz law and is further investigated by Brandt and Neuer [16]. Where the main conclusion was a 6% uncertainty when converting electrical resistivity to thermal conductivity. Figure 3 shows the resistivity of aluminium and alloys regarding temperature. The sudden increase in resistivity correlates to the melting temperature of the alloys. This correlates to approximately a 30% increase in resistivity when aluminium and alloys transition from solid to liquid.

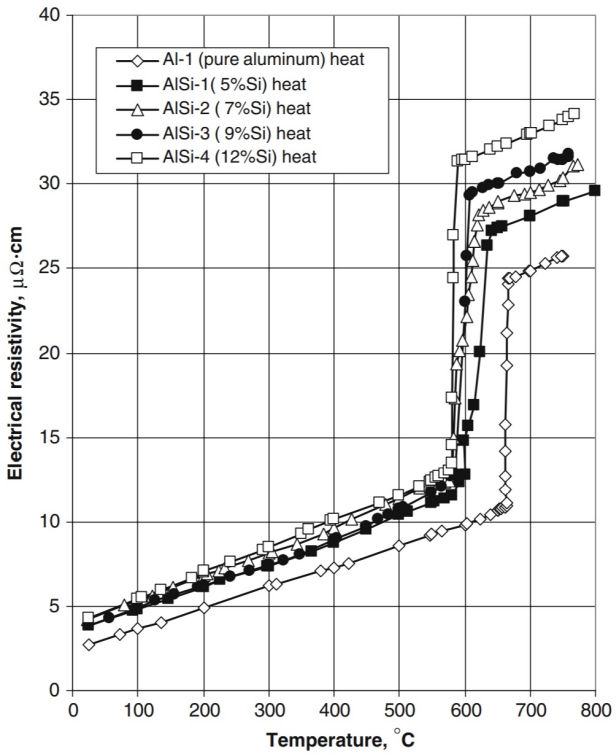

Figure 3: Electrical resistivity of pure aluminium and alloys [16].

2.2 Permanent magnet

The permanent magnets used during the trials are made of a neodymium iron boron alloy (NdFeB) and are encased in a stainless steel shell. They have an operating temperature of up to 323 kelvin ($50°C$), approximately around the Curie temperature, and inner magnetization of around 1.45T. These magnets are carefully manufactured to achieve the desired magnetic and thermal properties. A general process route for them includes creating an alloy from neodymium, iron and boron, grinding the alloy to powder, and pressing it to a desired shape. They are then sintered, machined and coated before they are magnetized by a strong magnetic field [4, 1, 24].

From Beinerts et al. [20] properties and grades of modern permanent magnets are accounted for. This is shown in Table 4 and 5. Here, the relations between operating temperature and inner magnetization can be determined. The specific magnet used in the project is N5211.

Table 4: Properties and grades of NdFeB magnets [20].

Type	Inner Magnetization, Br, T	Max. Operating Temperature K (°C)
N35AH	1.18	493 (220)
N38EH	1.22	473 (200)
N3825	1.25	453 (180)
N4220	1.3	423 (150)
N4517	1.34	393 (120)
N4816	1.38	373 (100)
N5014	1.42	353 (80)
N50M	1.46	353 (80)
N5211	1.45	323 (50)

Table 5: Properties and grades of SmCo magnets [20].

Type	Inner Magnetization, Br, T	Max. Operating Temperature K (°C)
S2415	1.00	523 (250)
S2610	1.05	573 (300)
S2816	1.10	573 (300)
S3212	1.15	573 (300)
S33.15	1.17	573 (300)
YXG32H	1.10	623 (350)
EEC24	1.02	673 (400)
EEC20	0.93	773 (500)
EEC16	0.85	823 (550)

2.3 Magnetic field theory

Magnetic fields are generated by moving electrically charged particles. Every field depends on a dipole, going from the positive north pole to the negative south pole. The magnetic flux lines will therefore move from the north pole to the south pole of the magnet [24], this is illustrated in Figure 4.

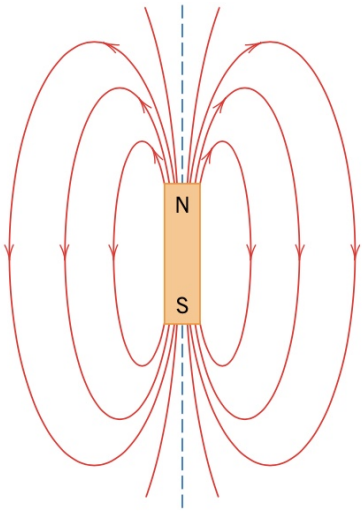

Figure 4: Magnetic flux travelling from the north pole (N) to the south pole (S) [24].

A magnetic field is usually denoted by **H** when talking about magnetic currents. When the focus shifts to effective magnetic poles, meaning permanent magnets, it is usually denoted by **B** [11]. The actual definition of these two fields is the following. **H** is an external magnetic field which can provoke a magnetic response in materials by aligning magnetic domains and is measured in $[\frac{A}{m}]$. **B** is the field that is generated as a response to a material being subjected to an **H** field, it is the magnetic flux density and is measured in Teslas [24]. Using Equation 3, magnetic flux density and magnetization can be linked.

$$B \cong \mu M \tag{3}$$

Where **B** is magnetic flux density [T], μ is the permeability $[\frac{H}{m}]$, and M is the magnetization $[\frac{A}{m}]$. The relation between **B** and **H** field is determined in Equation 4 [24], where $\mu = \mu_0 \mu_r$.

$$B = \mu_0 \mu_r H \tag{4}$$

μ_r is the relative permeability and is unitless, μ_0 is the permeability of free space with a given value of $4\pi \cdot 10^{-7} \frac{H}{m}$ [22]. This will indicate the degree to which a **B** field can be induced in the material in the presence of an **H** field. It also indicates the magnetic behaviour of the material, if $\mu_r < 1$ the material is diamagnetic, and if $\mu_r > 1$ the material is paramagnetic [24]. Furthermore, if $\mu_r >> 1$ the material is ferromagnetic. However, from the University of Iowa [22], the permeability of aluminium and the permeability of free space are almost the same. Therefore, the relative permeability of aluminium is approximately 1.

Relation between **B** and **H** field can be shown using a hysteresis curve in Figure 5. Here, two loops are related to a hard magnet and a soft magnet. A hard magnet has a big coercive field, meaning the width of the loop, this also means that it has a large permeability. For a soft magnet, it is the opposite. Hysteresis can be described as the history and the dependence of the state of a system [24].

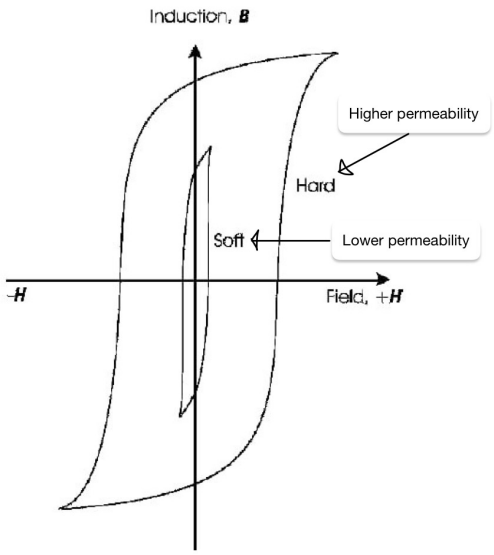

Figure 5: Hysteresis curve of a hard and soft magnet from [21] page 380.

2.3.1 Fundamentals of AC motors

When researching relevant theory for the project concerning rotating permanent magnets, the basic fundamentals return to the principles of AC motors. The U.S. Department of Energy made the handbook; "DOE FUNDAMENTALS HANDBOOK ELECTRICAL SCIENCE" [12], where the principles will be presented. These fundamentals are regarded as:

The operational principles underlying all AC motors are predicated upon the dynamic interplay between a rotating magnetic field generated within the stator via alternating current (AC), and a counteracting magnetic field either induced within the rotor or externally supplied via a distinct direct current (DC) source [12]. This interaction is shown in Figure 6. Here, points from T1 to T7 are shown with a 60°shift in position, resulting in a 360°rotation. T1 to T4 is described in Table 6, whereas T4 to T7 is the same process with opposite polarity as T1 to T4.

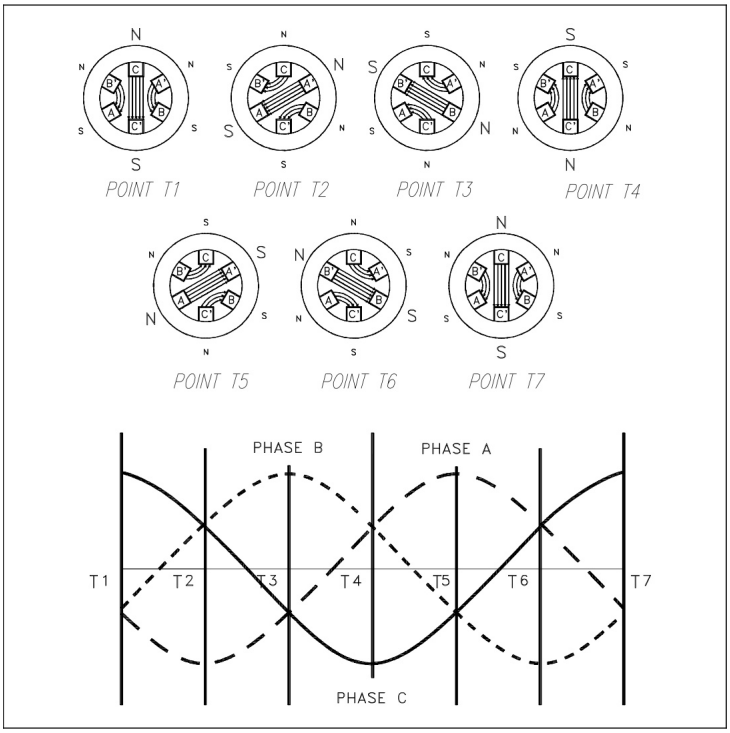

Figure 6: Principals for AC magnetic field in a motor [12].

Table 6: Description of AC-motor theory based on Figure 6 by The U.S. Department of Energy [12].

Time Point	Description
T1	At time point T1, phase C current reaches its maximum positive amplitude, while phases A and B currents are at half of their maximum negative amplitude. This configuration produces a downward-oriented magnetic field, strongest across phase C (between poles C and C′), reinforced by weaker fields across phases A and B (with poles A′ and B′ as north poles and poles A and B as south poles). Source: [12]
T2	At time point T2, currents in phases A, B, and C have rotated 60°. Phase A current reaches its maximum negative value, phase B current reverses direction and is at half of its maximum positive value, and phase C current decreases to half of its maximum positive value. This results in a leftward-oriented magnetic field, strongest across phase A (between poles A′ and A), aided by weaker fields across phases B and C (with poles B and C as north poles and poles B′ and C′ as south poles). Source: [12]
T3	At time point T3, currents have rotated another 60°, summing to a total rotation of 120°. Phase B current reaches its maximum positive value, phase A current decreases to half of its maximum negative value, and phase C current reverses direction and is at half of its maximum negative value. The resulting magnetic field is upward and leftward, strongest across phase B (between poles B and B′), assisted by weaker fields across phases A and C (with poles A′ and C′ as north poles and poles A and C as south poles). Source: [12]
T4	At time point T4, after a 180° rotation from T1, phase C current returns to its maximum value but with reversed polarity, establishing an upward-oriented magnetic field between poles C′ and C. Source: [12]

2.3.2 Rotating permanent magnet

A permanent magnet creates a static magnetic field, called a direct current field, or DC field. However, when the magnet rotates around its central axis it will create an alternating magnetic field, also known as an AC field. Using the knowledge from 2.3.1 this will induce a sinusoidal current shape with shifting polarity as shown with AC motors in Figure 6. Regarding this, a rotating permanent magnet will produce Lorentz forces, as a reaction force to the induced current in the metal close to the rotating magnet. This is similar to the more known theory behind electromagnets and electromagnetic pumps (EMP) which Fritzsch has investigated [7, 17].

2.3.3 Lorentz forces

When an AC magnetic field induces a current density into a conductive medium, the resulting Lorentz forces are observed to be perpendicular to both the magnetic flux and the current density [6]. Regarding this, the theory of AC magnetic fields can be applied to describe the Lorentz forces induced by rotating permanent magnets. The theory of Lorentz force is based on the premises of AC coils described by Fritzsch [7]. Lorentz force can be visualized at a single point using the right-hand rule, this is shown in Equation 5 [7] and illustrated in Figure 7.

$$\vec{F} = \vec{J} \times \vec{B} \tag{5}$$

Where $\vec{F}$ is the Lorentz force, $\vec{J}$ is the current density, and $\vec{B}$ is the magnetic flux. However, this is a simple way of illustrating the magnetic field and Lorentz forces.

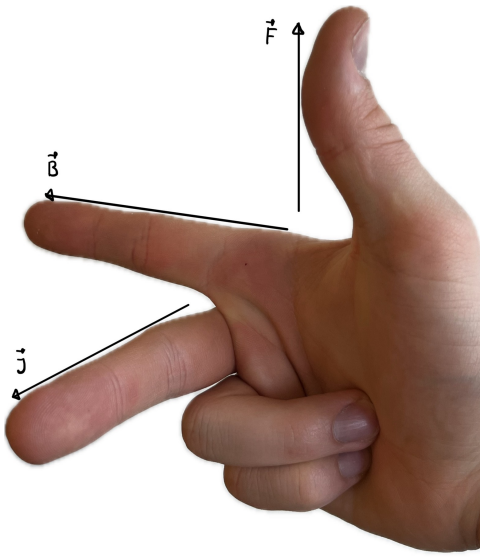

Figure 7: Lorentz force illustrated by the right-hand rule.

The current density, $\vec{J}$, is described by Ohm's Law for Electromagnetics [5] shown in Equation 6, where $\vec{E}$ is the electric current density and σ as before, is the electrical conductivity.

$$\vec{J} = \sigma \vec{E} \tag{6}$$

2.3.4 Gaussmeter

The Gaussmeter is a device for measuring magnetic fields using a phenomena called Hall effect. The Hall effect is observed when a conducting specimen, which is under the effect of an external electric field, is subjected to a magnetic field normal to the electric field. This will cause the charge carriers in the specimen to deflect and move in the direction normal to both the electric and magnetic fields,

giving rise to the Hall voltage. The Hall voltage V_H depends on the current I_x, the thickness of the specimen d, the Hall coefficient R_H, and the magnetic field B_z detailed in Equation 7 [21, 24, 8]:

$$V_H = \frac{R_H \cdot I_x \cdot B_z}{d} \tag{7}$$

From the equation, it is possible to see that the V_H is dependent on the angle between the magnetic field and the specimen. An angle of 90° will give the most accurate readings of a magnetic field because the Hall voltage will always be normal to the incident magnetic field. This means that to measure a magnetic field, the Hall plate of a probe from the Gaussmeter has to be normal to the magnetic field lines [8]. An illustration of the Hall effect is shown in Figure 8.

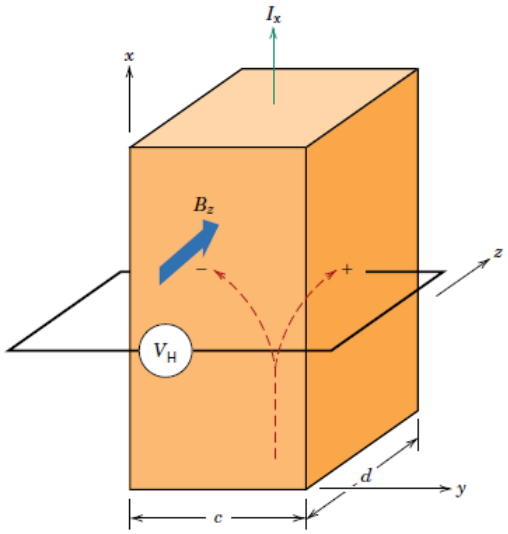

Figure 8: The Hall Effect demonstrated. A current is going through the specimen in the x-direction while a magnetic field is imposed in the z-direction resulting in a deflection of the charge carriers in the y-direction, found on page 70 in Callister et al. [24].

Hall plates are generally semiconductors because they provide much greater sensitivity than conventional conductors such as copper or gold. These plates are usually very small and therefore are easily affected by stray fields and poor angling of the probe. Common probe designs are axial and transverse probes shown in Figure 9. Axial probes are designed to measure field lines parallel to the tip, while transverse probes are designed to measure fields normal to the tip. Measurements taken at one point of the magnet are only valid for that point and not the entire surface of the magnet [8].

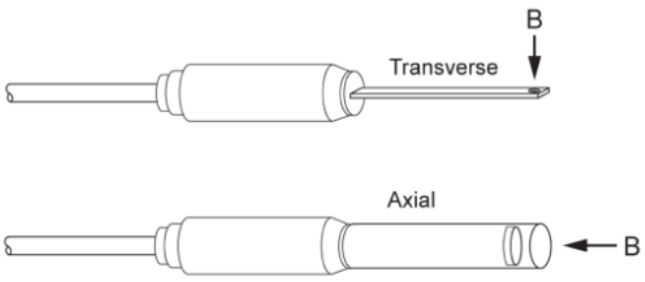

Figure 9: Common probe types for Gaussmeters [8] figure 5 page 3.

2.3.5 Penetration depth

When investigating the effect of the AC magnetic field on aluminium it is important to consider the penetration depth of the magnetic field into the aluminium. The electromagnetic penetration depth is defined as the distance over which the magnitude of the magnetic field is reduced by $1/e$ or a factor of 0.368 at a given change of polarity, here defined as the frequency (f). It further depends on the medium's resistivity and relative permeability and the permeability of free space, which all can be seen as constants [7, 17, 6]. Penetration depth is given by Equation 8.

$$\delta_c = \sqrt{\frac{\rho}{\pi \mu_0 \mu_r f}} \tag{8}$$

δ_c is the electromagnetic penetration depth, ρ is the electrical resistivity, μ_0 is the permeability of free space, μ_r is the relative permeability of the medium penetrated, and f is the frequency of change [Hz] of the polarity of the magnet. From Equation 8 it is shown that the penetration depth is inversely proportional to the frequency. When frequency increases the penetration depth decreases, this is because the alternating field will not be able to penetrate deep into the medium before a change of polarity at higher frequencies occurs. This results in the magnetic flux and currents accumulating near or at the conducting medium's surface, and is known as the skin effect [6]. The magnitude of an electromagnetic wave propagating through a lossy media is proportional to:

$$e^{-\alpha \cdot l} \tag{9}$$

Where α is the attenuation constant, and l is the distance travelled. This can be defined in terms of the penetration depth, which as mentioned earlier is defined as the distance where the field is reduced by a factor of $1/e$, to create the following formula [6]:

$$e^{-\alpha \cdot \delta_c} = \frac{1}{e^{-1}} \tag{10}$$

From Equation 10 the following is derived [6]:

$$\delta_c = \frac{1}{\alpha} \tag{11}$$

Using Equation 10 and Equation 11, an expression for the diminishing magnetic field through a material as a function of distance through the material can be defined as:

$$e^{-l/\delta_c} \tag{12}$$

The complete calculation can be found in Appendix D

2.4 Pumping of liquid aluminium, the premise of magnetohydrodynamics

Regarding Magnetohydrodynamics (MHD), the project sets out to verify the use of PMP on LML. This will then correlate to generation of MHD, describing the flow of an electrically conductive fluid inside a changing magnetic field. MHD is more thoroughly investigated by Kolesnichenco et al. and Pavlovs et al. [9, 23] and is only used as references in this thesis. As a part of the conclusion from Kolesnichenco, they claim that the interaction of multiple fields significantly alters turbulence behaviour. The increased amplitude of one field combined with a constant rotating field leads to decreased turbulence intensity. This suggests a potential for controlling wall turbulence by manipulating these fields, with implications for various applications. The main conclusion from Pavlovs states that an increase in magnetic field leads to increased surface area of influenced liquid metal. Beinerts et al. have previously shown that it is possible to use permanent magnets to pump liquid Galinstan (InGaSn) [20]. Galinstan has a melting point of 284 K, proving easier experimental work, and electrical conductivity of $\sigma = 3.3 \cdot 10^6 S/m$, and density of $\rho = 6400 kg/m^3$ [2]. The electrical conductivity is then approximately 70% to 90% lower than the aluminium used in this project.

In today's industry, pumping of liquid aluminium is usually done with EMPs, this is because liquid aluminium is highly corrosive. Mechanical pumping is the cheapest alternative, but requires regular service and replacement of impellers, while the impellers dissolve into the melt, introducing

undesired impurities into the aluminium. Using a magnetic field however completely removes this problem because the induction coils can be mounted on the outside of the pipes. The problem that arises with EMPs is the power consumption of maintaining an alternating current through the coils, while the coils require continuous cooling, usually established by a water cooling rig with large water-to-air blast radiators to remove the excess heat. The overall utility intensity of EMPs might be considered a downside of the system.
Another option for liquid aluminium is using PMPs. These pumps do not need an alternating current to create a magnetic field as they generate a field through their ferromagnetism. An issue with the magnets themselves is that they do not generate an alternating field. This means that the liquid aluminium will not be moved because no current will be induced when the magnet is idle. The solution to this is rotating the magnets, causing the field to alternate with respect to the liquid aluminium. Using PMPs requires noticeably less power to maintain, as it requires only a motor, rotating the magnet, compared to EMPs, but it sacrifices some control over magnetic field strength. When working with PMPs, the temperature of the system is also critical, as PMs have a curie temperature, where they would lose their magnetization.

2.5 Induction Heating

In the statement regarding rotating permanent magnets' similarities to electromagnetic motors and coils, it is possible to regard the same effect of induction heating using rotating permanent magnets. By doing this, the AC magnetic field of a magnet and a coil attains the same outcome of forces. The only difference, however, is the geometrical shape of each. Then, the rotating permanent magnet will be regarded as an induction heater when inducing an AC magnetic field on a conductive medium [15]. When calculating the calorimetric effect of the magnets' influence on a water-cooled aluminium billet, the calculations are done using the properties of water and the effect the aluminium billet applies to the water. Calorimetric calculations are done using constant pressure. This is given in Equation 13 [24].

$$q_{calorie} = mC_s\Delta T \tag{13}$$

Where $q_{calorie}$ is the calorimetric energy [J], m is mass [kg], C_s is the specific heat capacity [$\frac{J}{kg \cdot K}$], and ΔT is temperature change [K]. Equation 13 is alternated concerning mass flow, which is given in Equation 14.

$$Q = \dot{m}C_{s,w}\,\Delta T \tag{14}$$

Here, Q is the effect [W], $\dot{m}$ is the mass flow of water [$\frac{kg}{s}$], and $C_{s,w}$ is specific heat capacity of water [$\frac{J}{kg \cdot K}$]. Equation 13 and 14 is valid when assuming the aluminium billet has the same effect on the water, as the magnets' effect on the aluminium billet. This simplified method accounts for input and output values, excluding the transition between them.

3 Experimental approach

The thesis work is linked to magnetism, material properties and the interactions of electrical and mechanical parameters. An experimental test rig was designed and built to gather performance data on these interactions. In the following section, shown in Figure 10, details about the whole process, from the design of the test rig to how the measurements were done, are explained.

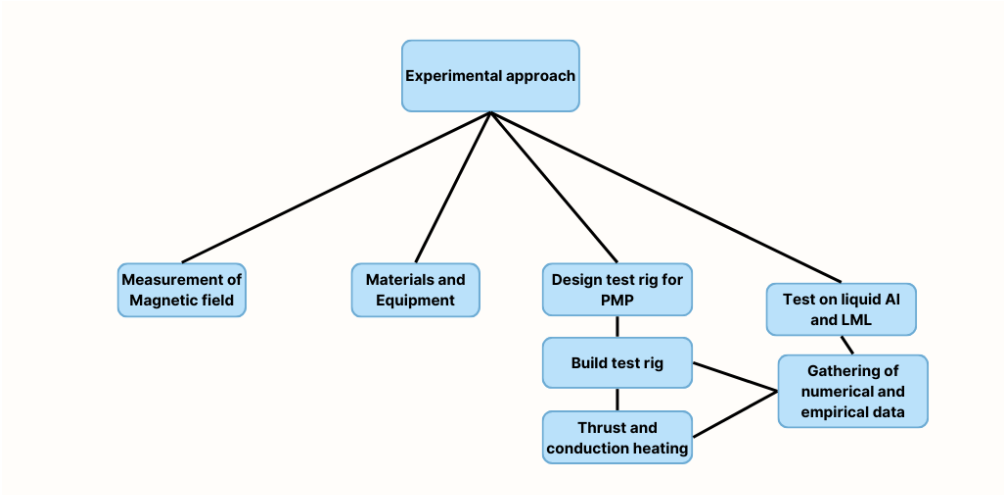

Figure 10: Flow chart describing the content for the experimental approach.

3.1 Materials and Equipment

The following table comprises a list of the equipment and programs used during the thesis work. This excludes all screws, bolts, angles, aluminium profiles, and other consumable parts used:

Lab equipment:

- FUKE® 219 Multimeter
- Hall Effect Gauss Meter model 6010 supplied by Pacific Scientific OECO, F.W. Bell®
- Ohaus® Defender 3000 Scale
- Two K-type thermocouples
- ABB MT71B14-4 Motor
- Parker AC10 Series 10G-12-0100-BF Inverter
- 4 Channel Omega HH1384 Datalogger Thermometer
- Sartorius BL6100 Scale
- TE Connectivity Load Cell, 22.6kg Range, Compression Measure

Programs:

- Simple Datalogger
- TestController Multimeter Program
- D4I Thermometer
- COMSOL Multiphysics® 5.5

Materials:

- Magnet, Neodymium iron boron (NdFeB) N5211
- Iron filings
- Aluminium billet (6082)
- Water cooled Aluminum billet (6060)

3.2 Measurement of Magnetic Field

Obtaining an idea of the magnetic flux field was necessary to find the magnet's optimal position during the upcoming experiments. Therefore, a testing scheme was designed for this purpose. For reproducible flux readings, a hole in the size of the magnet was cut into a Styrofoam plate and the distance was measured at 0cm, 1cm, 2cm, and 3cm shown in Figure 11 and 12. The measurements for the magnetic fields were taken using a Hall Effect Gauss meter model 6010. The different positions were measured by using the transverse probe from the Gauss meter as detailed in section 2.3.4

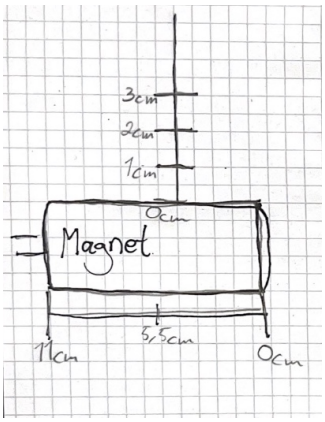

Figure 11: Rudimentary sketch of magnet and measurement points.

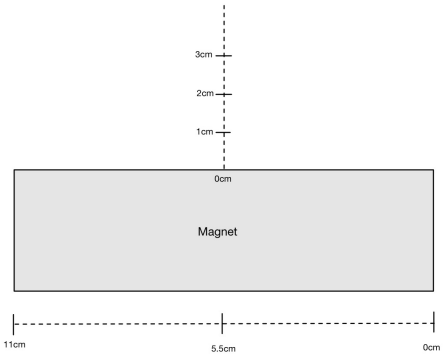

Figure 12: Digitized measuring points based on Figure 11.

Additionally, the measurements were taken at different lengths of the magnet, e.g. 0cm, 5.5cm, and 11cm, from the edge of the magnet, demonstrated in Figure 11 and 12. An assumption was made regarding the magnetic field theory of a dipole cylindrical permanent magnet. Hence, the measurements were taken at sides 1 and 2, as shown in Figure 14. An overview portrayed in Figure 13 shows how the depth and the height were measured with a plastic vernier to verify the correct position.

Figure 13: Gaussmeter-probe held in place with Styrofoam. Position controlled with vernier.

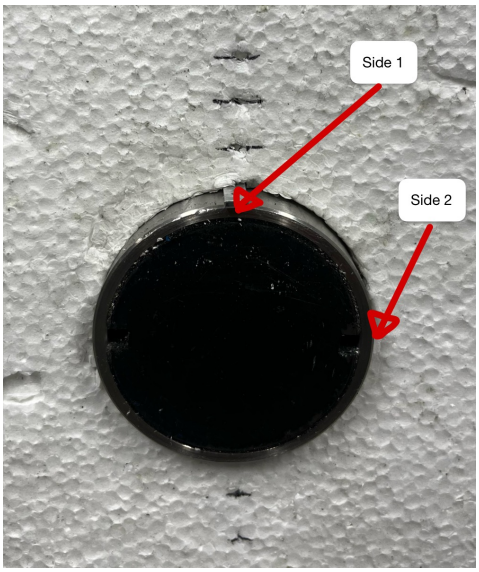

Figure 14: Magnet inserted in Styrofoam. Sides 1 and 2 were measured.

For visualizing the magnetic field, an experimental stand was designed. The stand was constructed using a wooden plank clamped to a table with two equally long pillars of wood placed normal to the first plank on top. A plastic plate with a sheet of white paper was placed on top of the planks. Then, a fine powder of iron filings was spread evenly on the paper. The magnet was then placed under the plate measuring 15cm from the top of the magnet to the bottom of the sheet of the plastic plate. The stand is shown in Figure 15, and a digital model is shown in Figure 16. When visualizing the field each side of the magnet was faced upwards and at different positions along the horizontal plank, the position was noted along with an image of the paper with the iron filings.

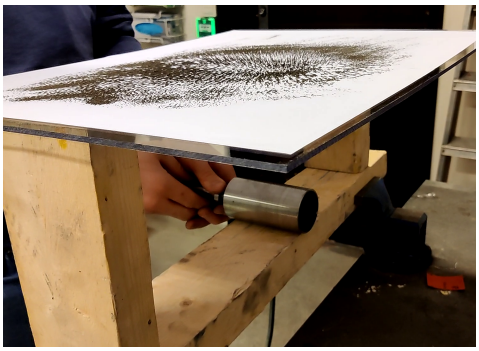

Figure 15: The testing setup for the magnetic field visualization using iron filings.

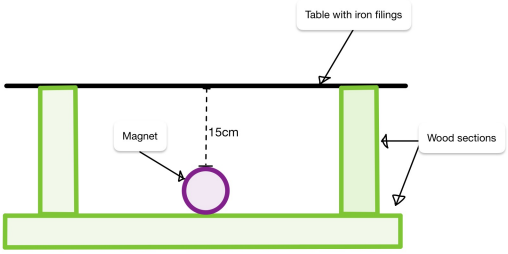

Figure 16: Front facing model for visualizing magnetic field with iron filings.

3.3 Building Test rig for PMP

Before the experiments with the LML, the performance parameters of a PMP must be determined. For this purpose, a test rig was constructed. The goal of the test rig was to gather accurate data about the effect of the changing magnetic field of the rotating PM on the solid aluminium billet. A conceptual sketch is shown in Figure 17. This design went through multiple iterations as errors arose, the following sections are an overview of the different iterations from first to final design.

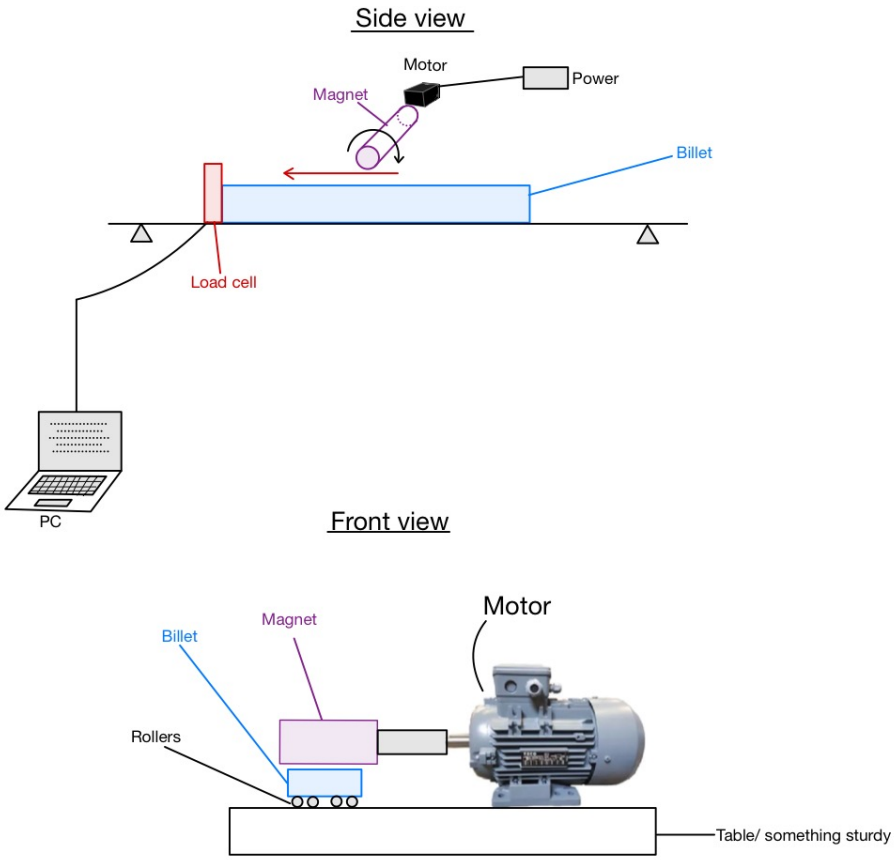

Figure 17: Rudimentary sketch of the first idea for the test rig.

3.3.1 First iteration

This was the first design envisioned for the test rig—a simple motor connected to a permanent magnet rotating over an aluminium billet (6082) positioned on rollers. A model was devised after some practical consideration and an overview of the available materials. The model would consist of two long aluminium frame sections going parallel with the intended direction of the billet functioning as the base of the rig. Two shorter frame sections at the end of the base would hold the load cell in place between them, and the motor would be positioned on the right side of the base held in place by two frame pieces. The model is shown in Figure 18.

Figure 18: Model of test rig constructed from aluminium frames.

The model was then built using bolts and screws to join the frame sections, which were cut from one-meter-long aluminium profiles Figure 19. In total, the rig consisted of sixteen individual aluminium frame sections which had to be measured and cut from the original four profiles Figure 20, and a couple of extra sections. The main reason for using screws and bolts was to make almost all parts of the rig adjustable and allow for quick assembly. This made the rig adaptable to different billets, magnets, and motors.

Figure 19: Measuring the cuts from a template piece.

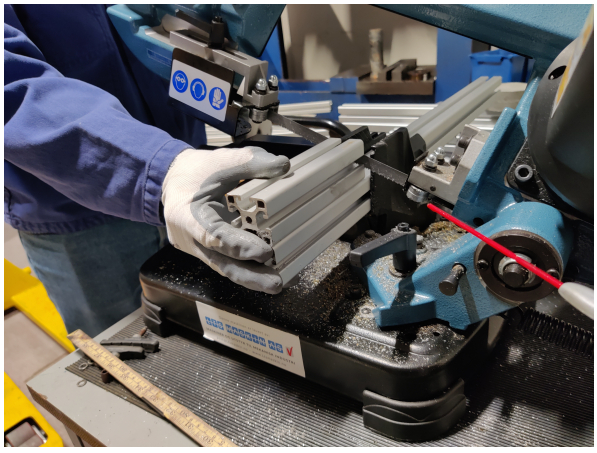

Figure 20: Cutting the aluminium profiles.

The base of the rig measured approximately 50cm long 15cm wide and 10cm tall Figure 21. The rollers were mounted on angled pieces that were fastened to frame sections, this allowed for easy adjustment of their position along the length of the rig. Adding the motor and magnet changed the dimensions of the rig to 50cm long, 40cm wide, and 35cm tall. The completed rig featured adjustable rollers, reinforced and adjustable magnet support with bearings, and a load cell which was fitted with banana plugs for direct connection to a datalogging multimeter. There were a couple of minor adjustments to the design during the construction, but the basic principle of the rig stayed the same throughout the entire process Figure 22.

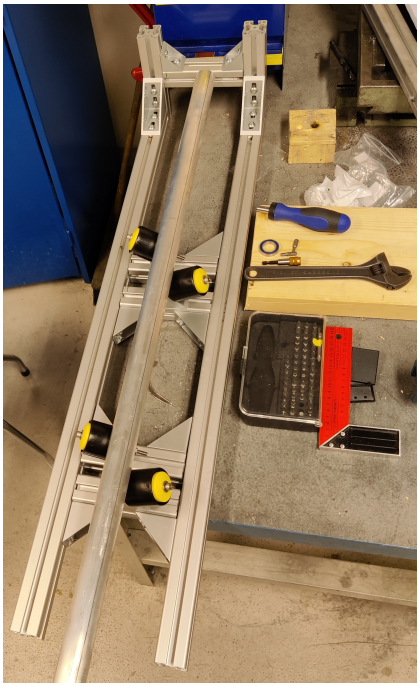

Figure 21: Rig without motor or magnet support.

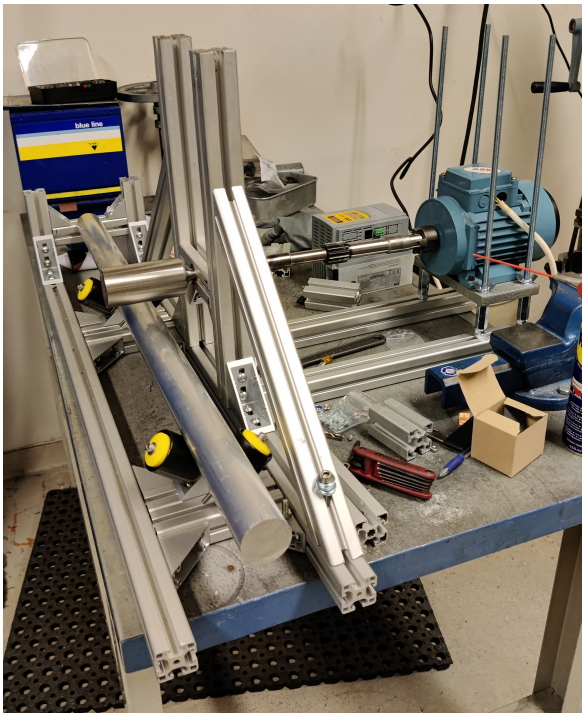

Figure 22: The completed first iteration of the rig.

The first iteration was not strong enough for the expected forces, and in addition, the motor had insufficient cooling when controlled by the inverter at low supply frequencies to allow for experiments longer than a couple of minutes. Therefore, a new motor was procured for the second iteration and additional reinforcement of the magnet support.

3.3.2 Second Iteration

The second iteration attempted to use a different motor but was unable to be mounted safely due to its design. Therefore, a new solution was devised using the old motor and a gear system.

3.3.3 Third Iteration

The third iteration had another supportive construction with a bearing connected to the axle Figure 23. A new shorter axle was procured and connected to a gear system which consisted of two five-tier pulleys and a fan belt shown in Figure 24. This allowed the motor to run at high RPMs, which is what it was designed for, while the magnet spun at a different set of RPMs, varying from low to very high speeds. The pulley system significantly increased the maximum possible RPMs for the entire rig. The motor was controlled by a Parker AC10 series inverter.

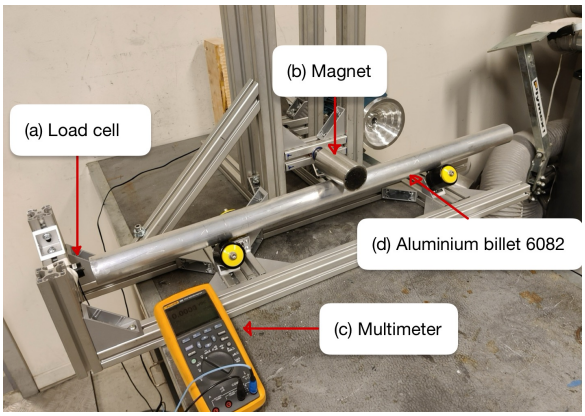

Figure 23: Overview of the third iteration of the rig. (a) is the position of the Load cell, (b) is the rotating permanent magnet, (c) is the FLUKE® multimeter, and (d) is the Aluminium billet (6082). The multimeter was connected to a computer for continuous data logging.

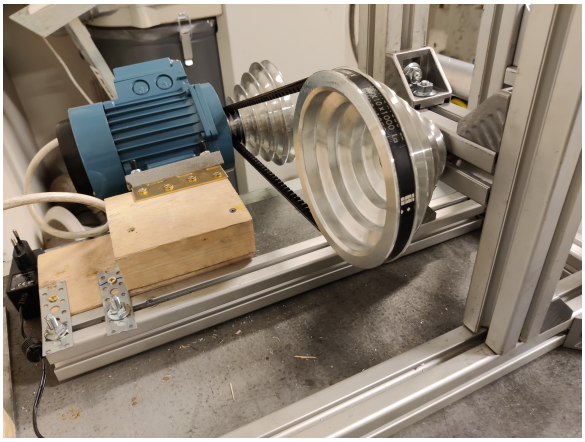

Figure 24: Gear system of the third iteration of the rig. Consisting of the motor and the five-tier pulleys with a fan belt connection.

3.4 Test approach for PMP test rig

The construction of the test rig resulted in two experiments, one test done on the thermal effect of induction in the aluminium, and the other on the correlation between the measured thrust and frequency of rotation at different heights above the billet. These tests will be known as the thermal test, and the thrust test respectively moving forward. Datalogging was done continuously throughout the tests using one computer connected to the different measuring equipment relevant to the test. All calculations were done using Python. The experiments were performed after one another with minimal modifications to the rig between them starting with the thermal test. It is important to note that the frequencies mentioned in the tests do not correspond to 1/s. These were the frequencies the inverter used as input to control the speed of the motor. A figure of the inverter's input frequency to the magnet's actual RPM at different gears is shown in Figure 25.

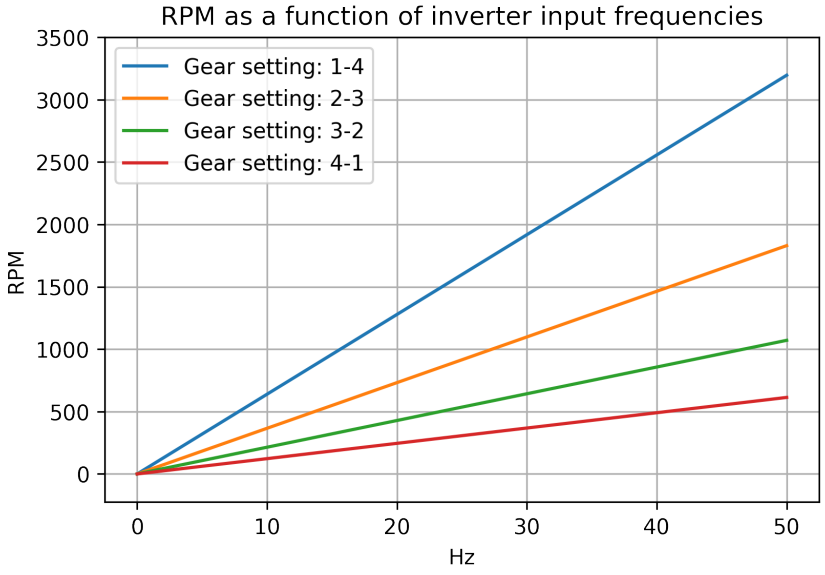

Figure 25: RPM of the motor as a function of input Hz in the inverter.

Table 7 shows the ratio between gears and their respective radii. These values, combined with a conversion factor from the motor were used to calculate the RPM of the magnet, this is shown in Appendix B. Figure 26 further illustrates how the pulley system worked. The fifth gear was left unused because the motor was unable to be fastened safely when using that gear.

Table 7: Gear settings used in the experiments with the corresponding diameters of the gearwheels.

Gears	First diameter [mm]	Second diameter [mm]
1-4	130.8	57.3
2-3	109.8	84.0
3-2	84.0	109.8
4-1	57.3	130.8

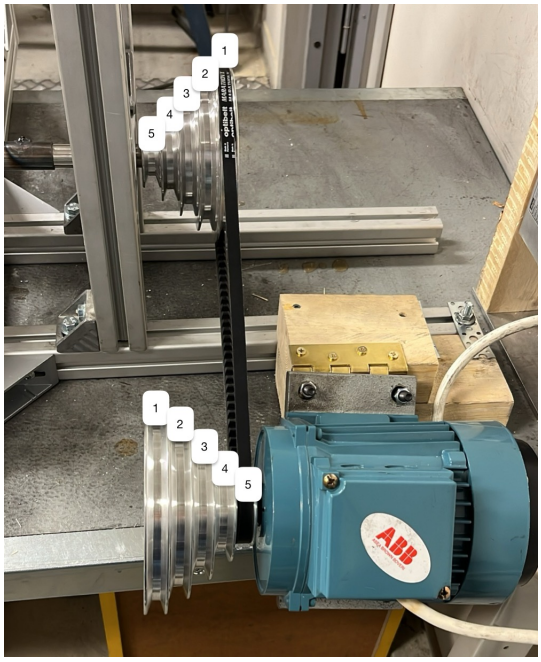

Figure 26: Five-tier pulley system with numbers indicating gears.

For further discussion and results, all speed-related rotations of the magnets are converted from RPM to Hertz by using; RPM/60s. This decision is based on the ease of use when all parameters are SI units.

In addition to the experiments performed with the test rig, a model of the system was made in COMSOL Multiphysics®. The finite element modelling (FEM) was supplied by Toms Beinerts, Institute of Physics of the University of Latvia. Parameters were adjusted and run by Robert Fritzsch and reviewed by the group using COMSOL Multiphysics® 5.5.

3.4.1 Test of thermal effect

A billet of aluminium (6060) was machined in the workshop to the dimensions, l = 260mm, d_o = 50mm and a hole in the middle, d_i = 8mm. Two water hoses have been mounted on the billet for a connection to water. The billet was placed in the rig and adjusted to fit the smaller size billet. Two thermocouples for accurate measurements were mounted inside the water hoses at each end of the billet. To avoid radiation losses the billet was protected by foam insulation on all sides leaving only a small space for the magnet. The load cell was moved to accommodate the shorter billet. The overview of this setup is shown in Figure 27. Prior to each trial, the water was run until the temperature reached equilibrium on both thermocouples. Then the motor was started and the test

began at a height of 0.5cm, model of position shown in Figure 28, inverter input: 50Hz at gear 1-4, and a rotation speed of 53.26Hz. Load from the load cell, water outlet weight for the flow rate, and temperature in and out were measured. All parameters were digitally logged using a computer. The test was then repeated with a height of 2.0cm, position shown in Figure 29, with the same rotational speed of 53.26Hz.

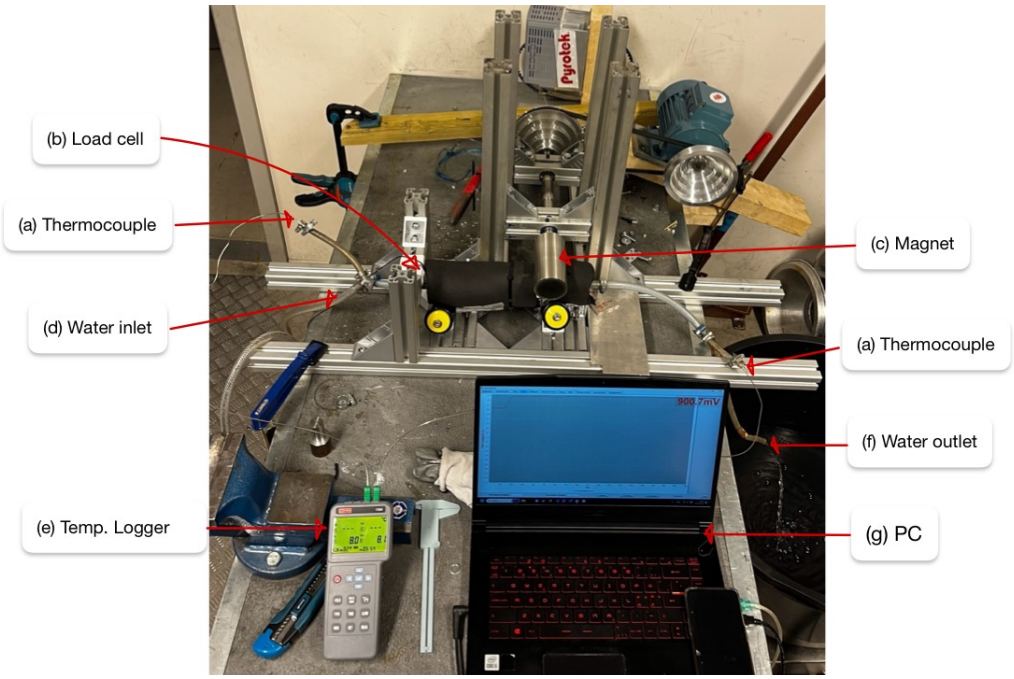

Figure 27: Induction test on Aluminium billet. The figure gives an overview of the setup. The test consists of (a) two k-type thermocouples, a (b) Load cell, a (c) rotating magnet, a (d) water inlet and an (f) outlet, a (e) Temperature logger, a Scale to measure the flow of water underneath the outlet, and a (g) PC for logging data from the load cell, water flow and temperature simultaneously.

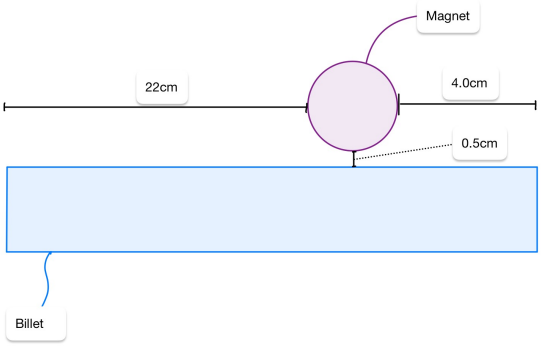

Figure 28: Model of the relative position of the thermal effect test, where the magnet was 0.5cm above the billet.

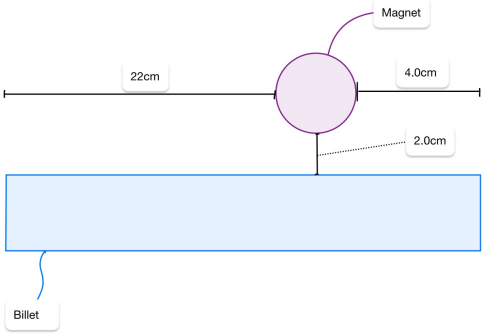

Figure 29: Model of the relative position of the thermal effect test, where the magnet was 2.0cm above the billet.

3.4.2 The thrust test

The thrust test was carried out by manually starting the motor, then increasing the inverter input ranging from; 40Hz, 45Hz, and 50Hz with 30-second increments at each speed. Then the gear ratio was changed and the same test sequence was repeated. Gearing was done at; 1-4, 2-3, 3-2, and 4-1. Specific speed in RPMs is shown in Figure 25. Height was also measured using several 0.5cm thick

aluminium plates, and the total experimental procedure was done at heights; 0.5cm, 1.0cm, 1.5cm, 2.0cm, 2.5cm, and 3.0cm. The maximum height of 3.0cm was regarded as an endpoint due to little effect on the load cell. The load was measured in millivolts [mV] using a load cell (TE Connectivity Load Cell, 22.6kg Range, Compression Measure) and a FLUKE® multimeter 289. Calibration of the load cell was done using weights of known mass using the load cell to calculate the force in [Kg] and [N].

3.4.3 Validation with liquid aluminium

Before mounting the rotating magnet system to the LML, validation, and proof of concept were performed. The test rig was moved to the melting lab where trials with liquid aluminium took place. A riser tube was cut and prepared in casting sand for support. In this configuration, the minimum distance obtainable to the magnet is 3.0cm. Most likely this distance will be greater than 3.0cm to avoid direct contact with the riser tube. This test was only conceptual and time was of the essence. Therefore, the riser tube was simply held over the spinning magnet, and recorded with a camera. The goal for this trial was to visually see the magnet's effect on liquid aluminium. Figure 30 and Figure 31 show the setup and how the riser tube is held.

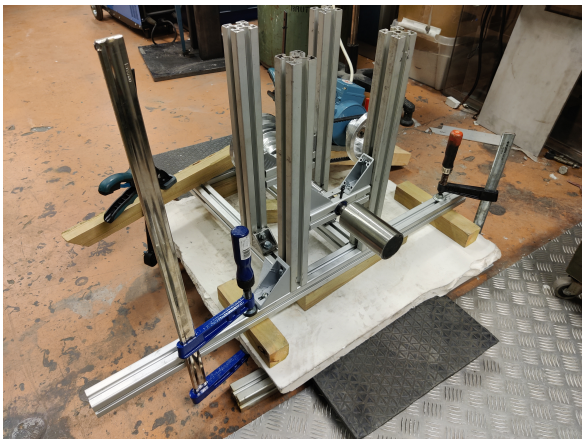

Figure 30: Setup for the preliminary liquid metal trials.

Figure 31: Visual setup of verification trial.

3.5 LML

The LML was designed and built by supervisors Robert Fritzsch and Paul Bosworth. Figure 32 is a CAD file of the LML. The LML consist of interchangeable modules for the flexibility of future experiments. Figure 33 shows the refractory where liquid aluminium will flow. While Figure 34 shows how the lids can be opened and closed for ease of work.

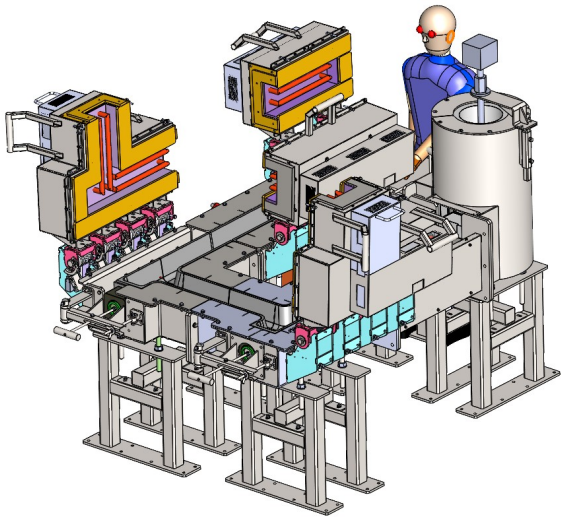

Figure 32: CAD of LML

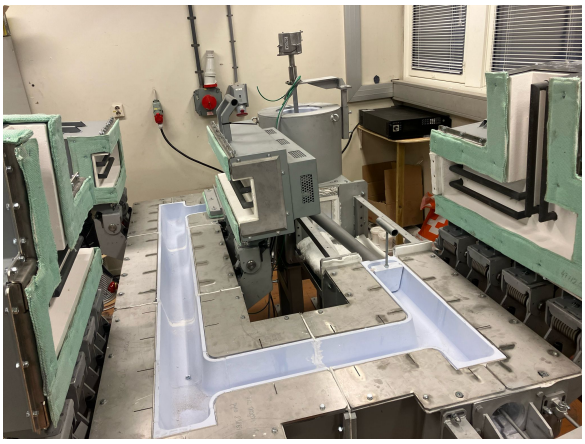

Figure 33: Overview of LML with one open lid and one closed.

Figure 34: LML with open lids revealing the refractory lane, and the heat elements in the lids.

Some additional adjustments were made to make the motor and magnet suitable for mounting on the LML. New bearings and a new connector replaced the old and more fragile components.

No more building was possible within the timeframe of the thesis work. This will be discussed further in the section on future work.

4 Results and Discussion

Results and discussion from this project will be presented and discussed here. This section consists of four main parts, shown in Figure 35, with most of the empirical results gathered from the test rig. Data from the test rig and observations from the validation test for liquid aluminium will be presented. Results from the FEM simulation will also be presented and compared to the experimental data. It is important to note that all mentions of frequency in this section relate to values that have been converted from RPM, using the correlation Hz = RPM/60, examples of conversions can be found in Appendix B.

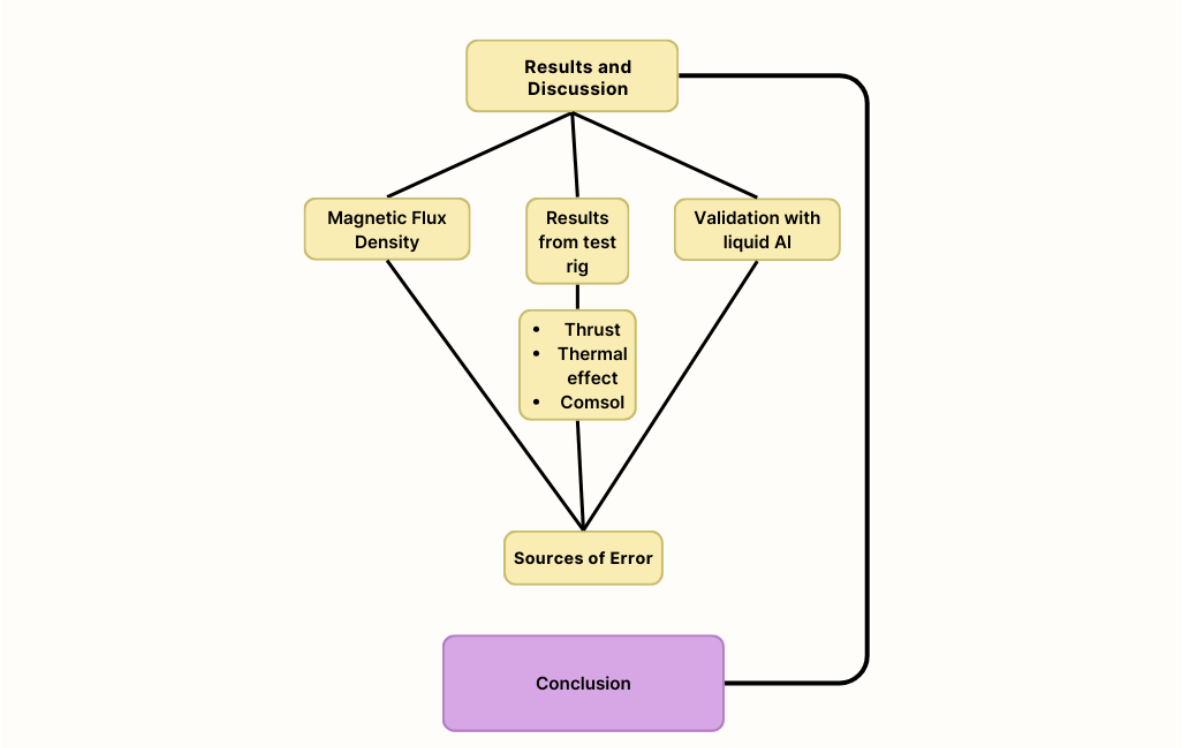

Figure 35: Flow chart describing the content for results and discussion.

4.1 Sources of Error

The experimental trials are susceptible to multiple sources of error. These will here be presented and discussed to elaborate on the impact of the results. For the magnetic field, positioning of the probe proved to be important, while readings were repeatable the source of error was estimated to be higher than the variance of the probe and Gaussmeter. Friction and vibration were the biggest visual and audible parameters observed during testing on the test rig. During the thermal effect trial, the temperature logger fluctuated more than expected, but with the same magnitude of each thermocouple. Forward is an overview of the trials and equipment that can indeed affect the results:

Experimental test:

- Measurement of magnetic flux
- Measurement of thrust
- Measurement of thermal effect
- Validation with liquid aluminium
- Plotting and data

Test equipment:

- Gaussmeter
- Load cell and multimeter
- Thermocouples and temperature logger
- Measuring tools

4.1.1 Measurement of Magnetic flux

For the measurement of the magnetic flux, the jig was cut out of Styrofoam, which is susceptible to deformation during the test. Also, the placement of the Gaussmeter probe should be as perpendicular to the magnet as possible. Most likely the probe was not in the most effective position during trials. However, this variance is estimated to be slightly higher than the error of the probe and Gaussmeter, both with a $\pm 0.25\%$ margin of error. Results from the test proved to be repeatable, therefore, variance in accuracy was negligible. A plastic vernier was used to verify the correct height and position, plastic was used because of the difficulties of using a steel vernier on a magnet. From the experience of operating the plastic vernier, the measurements are expected to vary with $\pm 0.1cm$.

4.1.2 Measurement of Thrust

During the trial for measuring thrust, several observations could have led to affected results. Firstly, the operation of the rig is prone to friction in several parts; the motor, slip of the fan belt and excessive tension, oscillation of the axle connecting the magnet, friction of the bearings, and friction from the rollers on the billet. A small rotation of the billet was observed during high-speed tests. Vibrations from the test rig can also introduce inaccurate results, e.g. a resonating movement on the billet, vibrations could also affect the height of the magnet. Bolts and screws are prone to untread and may cause slip in the system. Also, the Load cell produces an accuracy of ± 1 $\%span$ with an amplified span of ± 0.12 V divination from 4.0 V. The FLUKE® multimeter 219 has a 0.025% accuracy span when measuring DC volts. Comparing the different sources of error in this trial, it is evident that friction and other movements in the system are the biggest sources of error.

4.1.3 Measurement of Thermal effect

The trial measuring the thermal effect consists of many parameters that may affect the results. As well as the errors for the thrust test, the thermal effect test will add; variance of the two k-type thermocouples, Temperature logger, and heat dissipation from the billet to the surroundings. The 4-Channel Omega HH1384 Datalogger Thermometer has an accuracy of 0.01% of reading $\pm 0.1^{\circ}C$ per $^{\circ}C$. During the test regime, fluctuations of the temperature were observed to be approximately $\pm 0.5^{\circ}C$. This was one of the most inconsistent readings during the experimental trial, however, the two thermocouples measured within the $\pm 0.1^{\circ}C$ to each other. Therefore, ΔT varies with the same magnitude and will not affect the results more than the stated error of the temperature logger.

4.1.4 Validation with Liquid Aluminium

The validation test with liquid aluminium includes multiple sources of error. The test was performed by holding the liquid over the rotating magnet. This could have led to; inconsistent height above the magnet, vibration to the liquid, and flow of liquid due to uncontrollable movements. However, the experience and execution of Robert Fritzsch with liquid aluminium indicated a strong possibility for the proof of concept.

4.1.5 Plotting and data

Most of the following graphs that will be presented include trend lines and different curve fit calculations to fill the gaps between data points to anticipate further evolution. As such, there is a margin of error when displaying the data this way. Because many of these curve fits are the basis of discussion, the conclusions have to be verified and the error has to be known. To measure this, the squared value of R, also called the coefficient of determination is calculated. R-squared close to 1 means that the graphs are a good fit, while R-squared close to 0 means that it is a bad fit. R-squared is included in all graphs where it is relevant.

4.2 Magnetic Flux Density

The results gathered from the magnet were measured using a Gaussmeter, with values presented and arranged by the position in relation to the magnet. The two sides of the magnet were presented in Figure 14. Table 8 are measurements of side 1 of the magnet. This table reveals that the field is

denser when measured closer to the middle of the magnet's length. The magnetic field reaches its highest value of 0.561 T in the centre of the magnet's length at a height of 0cm. The magnetic flux decreases with increased distance from the measurements in Table 8.

Table 8: Magnetic flux, DC, side 1 of magnet.

Height [cm]	Lenght [cm]	Magnetic flux [T]
0	0.0 5.5 11.0	0.304 0.561 0.020
1	0.0 5.5 11.0	0.158 0.308 0.063
2	0.0 5.5 11.0	0.095 0.185 0.069
3	0.0 5.5 11.0	0.060 0.118 0.046

Table 9 is measurements taken on side 2 of the magnet. All measurements were low, with no correlation between the height and position of the test probe. As discussed in 2.3 and 2.3.4, the probe measures flux perpendicular to the probe head, in this case, side 2 should have horizontal flux lines that curve around the magnet. Therefore, the magnetic field is inconsistent and low in strength. While readings may occur due to interference and a slight angle of the probe, it is evident that the field of this side using this method should be zero. This statement is supported by the theory regarding the Gaussmeter 2.3.4.

Table 9: Magnetic flux, DC, side 2 of magnet.

Height [cm]	Length [cm]	Magnetic flux [T]
0	0.0 5.5 11.0	0.015 0.026 0.014
1	0.0 5.5 11.0	0.006 0.009 0.020
2	0.0 5.5 11.0	0.008 0.030 0.007
3	0.0 5.5 11.0	0.001 0.004 0.008

Figure 36 shows a plot of the magnetic field as a function of distance from the magnet. The graph is based on the measurements made from the middle of the magnet length at side 1. The heights at which the thrust test readings were measured are also marked with dotted black lines. Side 2 was not plotted since the magnetic field measured there is inconsistent and any readings of substance are likely a result of misalignment of the probe which does not represent the actual magnetic field, as detailed in 2.3.4.

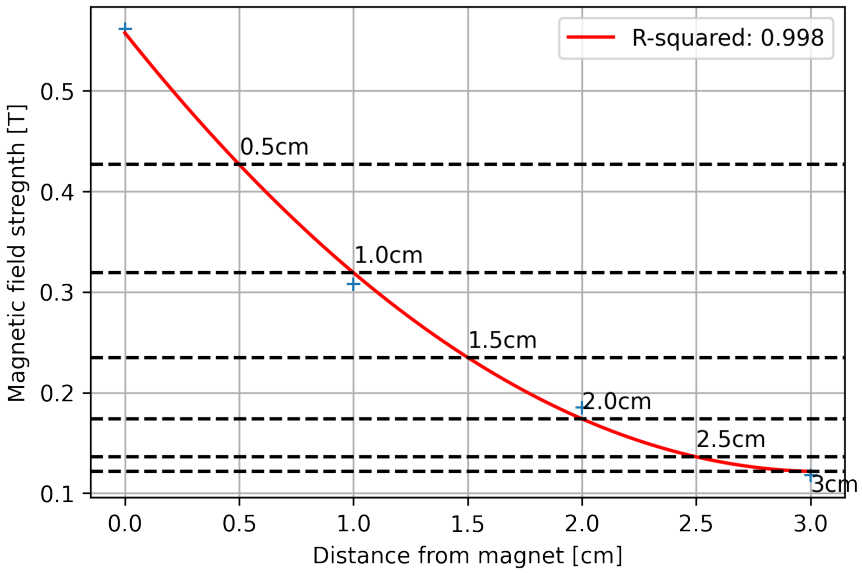

Figure 36: The magnetic field as a function of distance from the magnet. Measured from the middle of the length of the magnet (5.5cm) on side 1.

In addition to the measurements, there was also the visualization of the field using iron filings. From this test, several pictures were taken but only two were selected to represent each side of the magnet. With these images, it is possible to see the direction of the field lines at different points on the magnet. In Figure 37 side 1 points upwards, and the field lines exit vertically from the paper's middle and gradually angle outward farther from the middle. In Figure 38 side 2 points upwards, and the field lines are curving around the middle of the paper and, entering on one side while exiting on the other. These results confirmed the suspected position of the poles of the magnet visually, and the development of the field further out from the magnet.

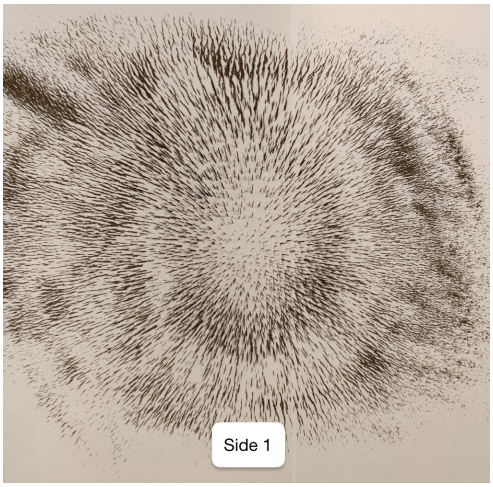

Figure 37: Magnetic field shown with iron filings from the "strong" side of the magnet, side 1.

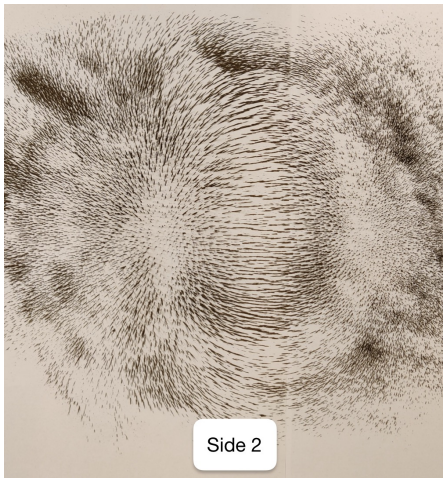

Figure 38: Magnetic field shown with iron filings from the "weak" side of the magnet, side 2.

4.3 Results from test rig

The results from the test rig are divided into results gathered from the thrust, thermal, and FEM simulation respectively. The reason for this order is that the thermal test yields results that are

better understood after first understanding the results from the thrust test. The results from the FEM simulation will be compared to the experimental results at the end.

4.3.1 Thrust

The test rig yielded many interesting results regarding the thrust from magnetic pumping. Shown in Figure 55a are the results from rotating the magnet 0.5cm above the billet. Graphs from the other heights can be found in Appendix C. The effect strongly depends on the distance from the aluminium, and it appears possible to reach a bigger thrust at higher frequencies than the tests were running at. This is best seen in the tests at 0.5 and 1.0cm above the billet. The effect of the rotation speed declines as the magnet reaches middling speeds, and around 45Hz it reaches a point where it seems to flatten out. This is more evident when looking at the derivative of the force with respect to frequency in Figure 55b. These graphs also speak to the efficiency of high-speed motors as they give an estimate of how much force the magnet induces per hertz.

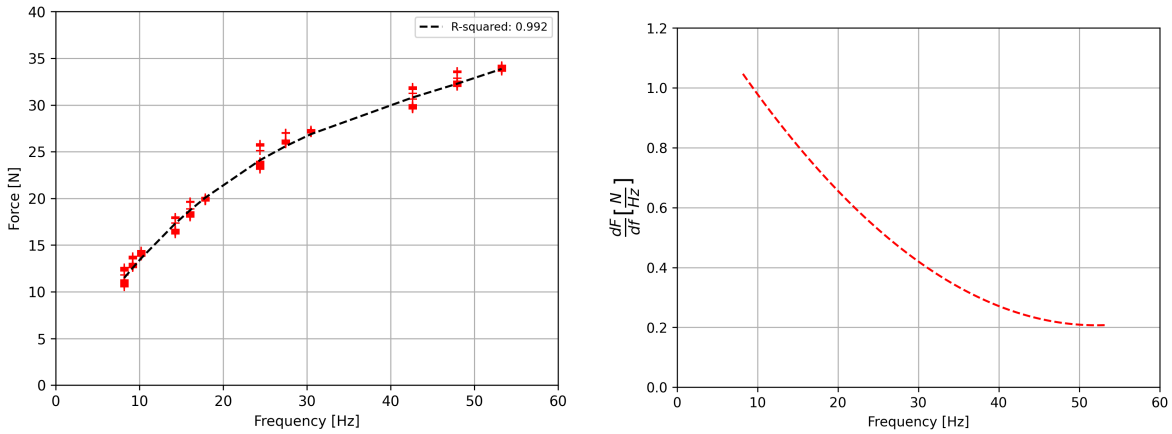

(a) Force readings at 0.5cm away from the billet.

(b) Derivative of the force readings 0.5cm away from the billet.

Figure 39: Plots of the force as a function of frequency at 0.5cm above the billet.

Figure 40 summarises all the thrust graphs across all the distances. Maximum thrust was measured to be 34.25N with a rotation speed of 53.26Hz, 0.5cm above the billet. The minimum thrust was measured to be 1.911N with a rotation speed of 8.18Hz, 3.0cm above the billet. This makes it possible to compare the distances between the force achieved at different heights with the measurements of the magnetic field made at those heights Figure 36. As expected there is a correlation between the distance from the billet and the thrust on the load cell. Each decrease of the magnetic field strength as a function of height corresponds with approximately the same decrease in force as a function of height per cent-wise.

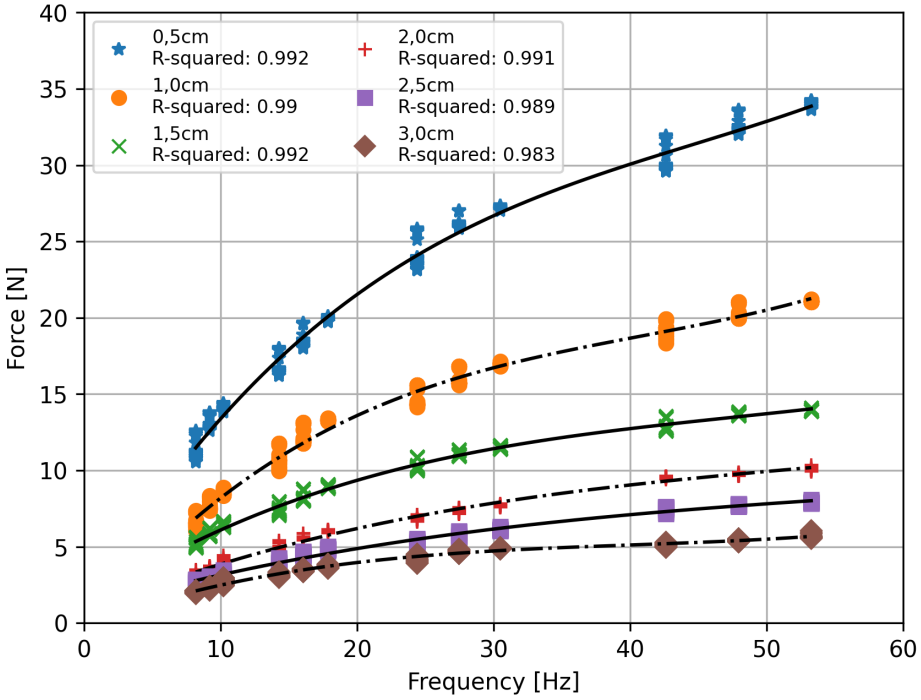

Figure 40: Thrust on the load cell as a function of frequency at different heights above the billet.

The penetration depth for the billets used in both the thrust and the thermal test were plotted using Equation 8 to investigate the decreasing thrust force within each height measurement. In Figure 41, the penetration depth of the magnetic field into the billet is shown as a function of the frequency of the rotating magnet, and marked on the x-axis as dotted black lines are the maximum and minimum frequencies where measurements were made. Within this range, the force decreases as the penetration depth decreases. For the billet used in the thrust test, the penetration depth varies between 3.5 to 1.5 centimeters.

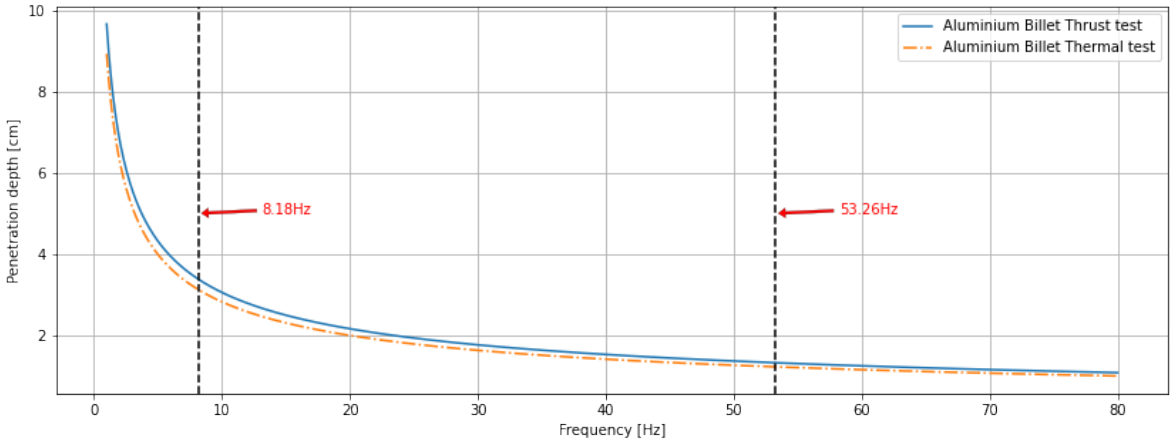

Figure 41: Plot of the penetration depth as a function of frequency. The black dotted lines indicate the maximum and minimum frequency measured in the thrust test.

Figure 42 shows how the force experienced by the billet on the surface develops as the field penetrates further into the bulk material. With the magnet spinning at 50Hz at a height of 0.5cm above the billet it shows the force as a function of distance into the billet. Each penetration depth represents a decrease in the thrust force of $1/e$, or around 37% of the value at the surface. In the case of Figure 42, the force reaches almost $1/e^4$ of the surface value.

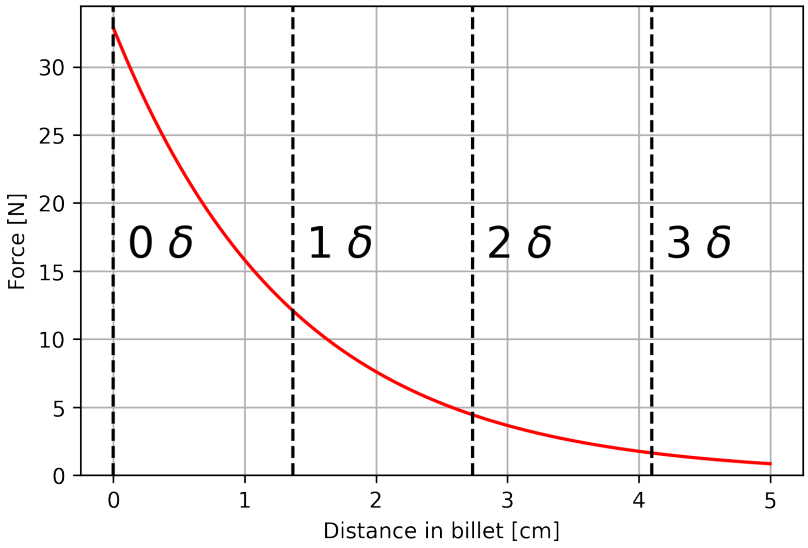

Figure 42: Force as a function of distance into the billet at 50Hz and with the magnet 0.5cm above the billet. Calculated using Equation 12. Different penetration depths (δ) are shown to the end of the billet, at 5cm.

The penetration depth will affect the distribution of the magnetic field in the billet, which will determine the induced current densities that induce the thrust forces measured. As these forces are dependent on the magnitude of both the magnetic field and the current densities as shown in Equation 5. The current density is dependent on the conductivity and the induced electric field shown in Equation 6. The magnetic field is dependent on the orientation of the magnet at a given time step, and it will accumulate near the surface of the billet due to the skin effect as discussed in 2.3.5.

Figure 43 shows the force and penetration depth as a function of frequency, the values presented for penetration depth are of the relevant scale for the billet. These graphs show the correlation between the penetration depth and the thrust force. In Figure 44 the force graph is inverted and shows that the two graphs almost overlap, meaning that the force correlates with penetration depth. This is likely due to the increased volume of interaction at high penetration depths, allowing for higher current densities which will result in more force throughout the billet.

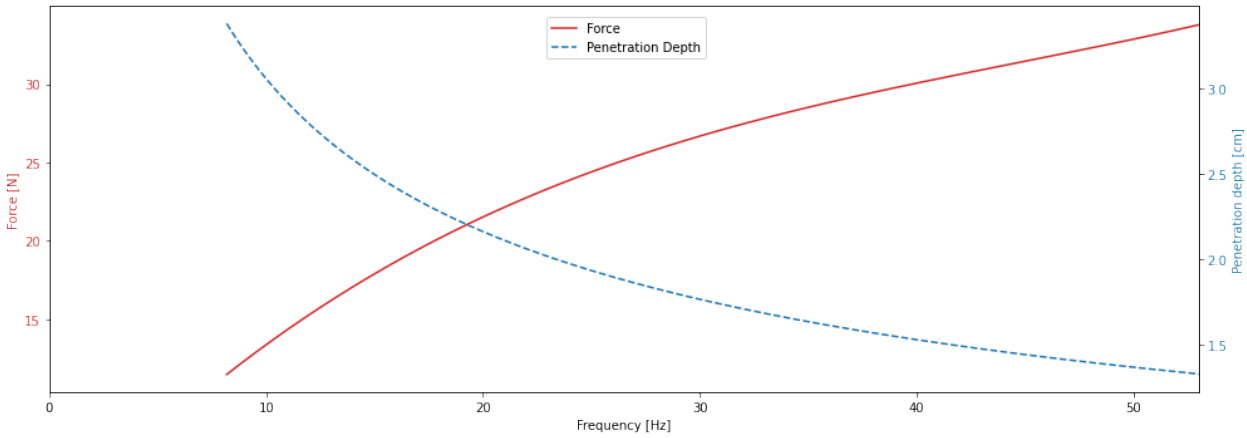

Figure 43: Penetration depth and Force readings plotted in the same figure, sharing the x-axis.

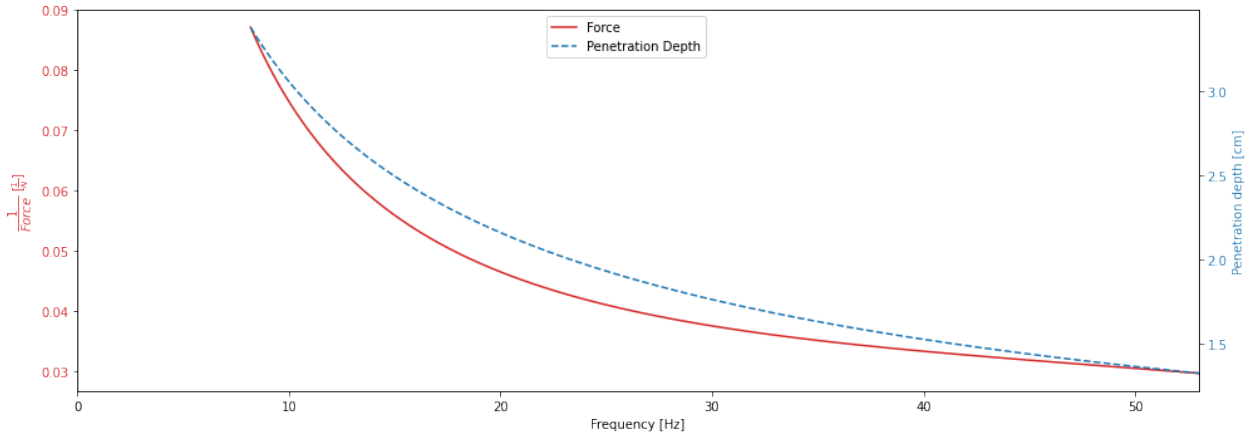

Figure 44: Penetration depth and the inverse of the force readings plotted in the same figure with a shared x-axis.

The results presented in this section speak to the effects and parameters related to the forces induced in the billet. For a billet with a given thickness, the determining factors for how effectively it can be moved mainly depend on the conductivity of the material, and the strength and frequency of the magnetic field. Because of its effect on the force distribution in the billet, the penetration depth is very important when designing and discussing the magnetic movement of materials.

This can be translated to liquid aluminium, where the resistivity will be greater, and the penetration depth will be bigger. In addition to the penetration depth, the liquid aluminium will be easier to move by virtue of being a liquid since the structure is much less rigid than a solid. These results therefore give a very good indication of the possibilities of liquid aluminium pumping using rotating permanent magnets.

4.3.2 Thermal effect

The thermal test yielded results of the inductive losses of the magnet. The data displayed in Figure 45 are used to calculate the heat losses related to the inductive forces using Equation 14, shown in Figure 46. Here, thermal test 1 averaged approximately 300W, and thermal test 2 averaged around 160W. Parameters of these tests are shown in Table 10.

Table 10: Parameters of the thermal test.

Test Nr.	Height above magnet [cm]	Speed [Hz]
1	0.5	53.26
2	2.0	53.26

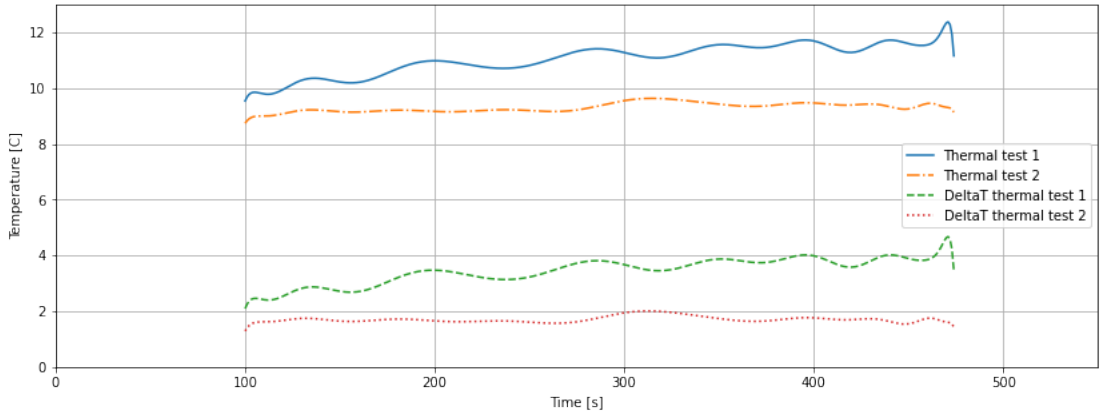

Figure 45: Temperature as a function of time for both tests, as well as the difference between temperature in - and temperature out of the billet. In the graph, only temperature out is shown and the heating up and cooling down regions are removed.

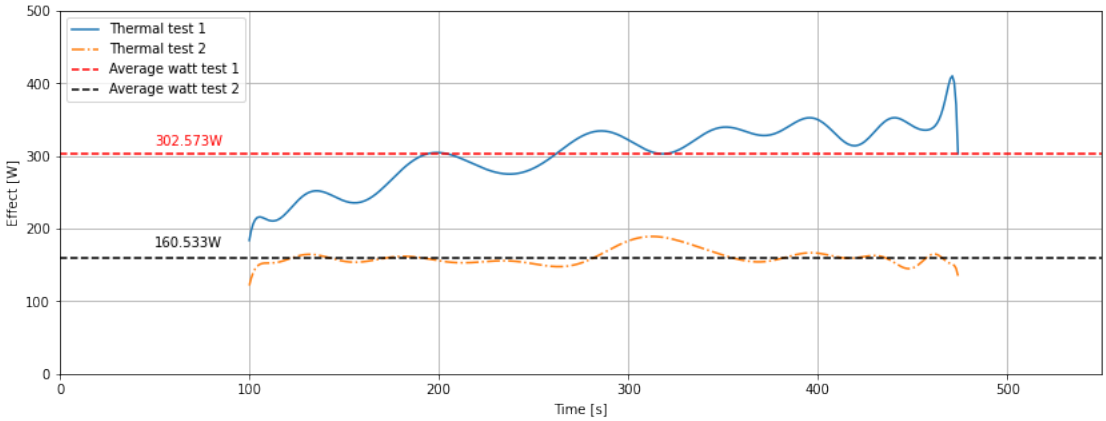

Figure 46: Heat loss expressed as watt as a function of time. As well as the average heat loss for the whole test. Test 1 was conducted 0.5cm above the billet, and test 2 was conducted 2.0cm. The graphs are edited to show only the results gathered from the equilibrium state of the system. Meaning the results from the heating up and cooling down of the billet are removed.

The thermal test revealed that a large amount of the energy added to the system is lost via the inductive heating effect that occurs in the aluminium. This is more pronounced closer to the billet as it experiences a stronger magnetic field. The heating effect itself is part of the total energy applied to the system, with the other major part being the effect that goes into the thrust force. As the total energy increases when the magnet is closer to the billet and the magnetic force acting on the billet is stronger, so does the heating energy. Calculating the effect of the force requires the total input into the system, which was not measured. The force during the thermal test was measured and can be seen in Figure 47. It is important to note that the billet used in the thermal test had a higher conductivity than the one used in the thrust test, and as a consequence, it reached a higher thrust force of 37.68N at a maximum frequency, of 53.26Hz, 0.5cm above the billet. The thermal test 2 reached a force of 12.64N, at maximum speed (53.26Hz), at 2.0cm above the billet.

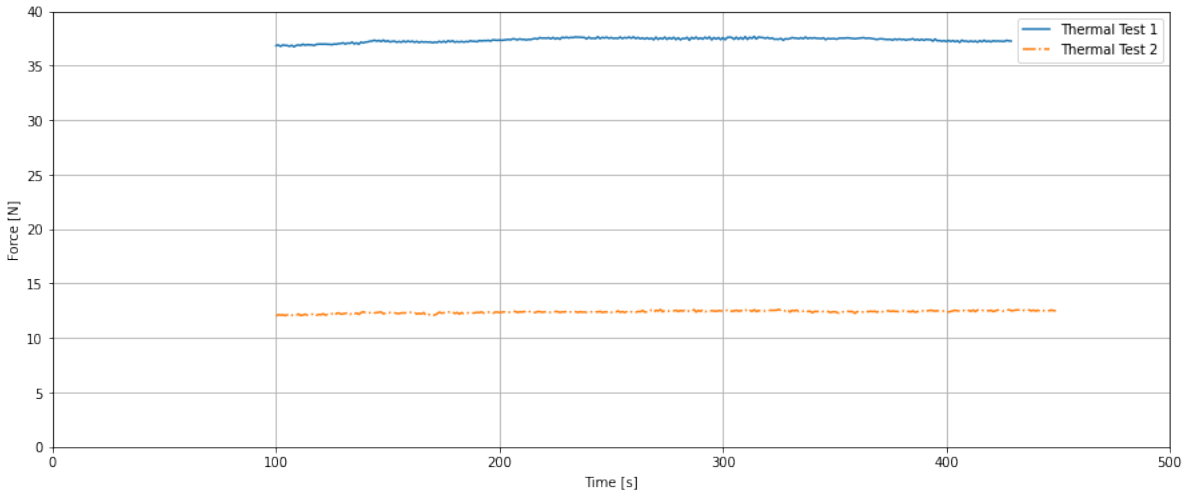

Figure 47: Force as a function of time throughout the thermal test experiment.

4.3.3 Comsol Multiphysics®

Provided by Toms Beinerts at the Institute of Physics from the University of Latvia a model of the test rig system in Comsol Multiphysics®. This is a simple model that assumes ideal conditions, as such a certain level of discrepancies and inconsistencies are expected.

The model shows promising results for the measured force and thermal losses. In Figure 48 the geometry of the entire modelled system is shown. An important difference between the model and the actual setup is that the magnet is placed below the billet. This was also considered for the test rig but was scrapped for practical reasons. Therefore, parameters are inverted compared to the experimental trial.

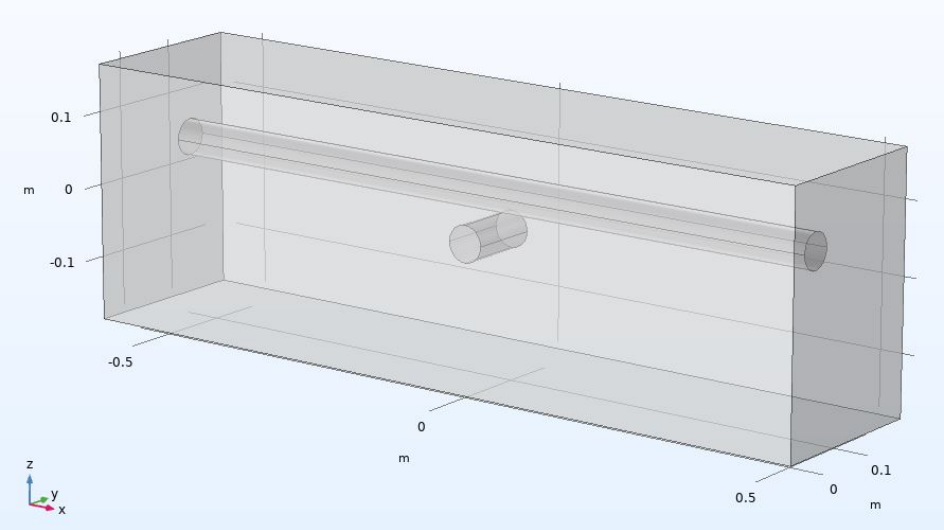

Figure 48: Comsol Multiphysics® model of the magnet and the billet used in the Finite element modelling (FEM) simulation.

In Figure 49 the face of the billet is shown looking down the x-axis, and the magnet is from the side. The magnet is rotating away from the viewpoint, as can be seen by the magnetic flux density represented by the arrows curving around and down on the other side of the magnet. Important to note is the minimal y-component of the flux density in the billet.

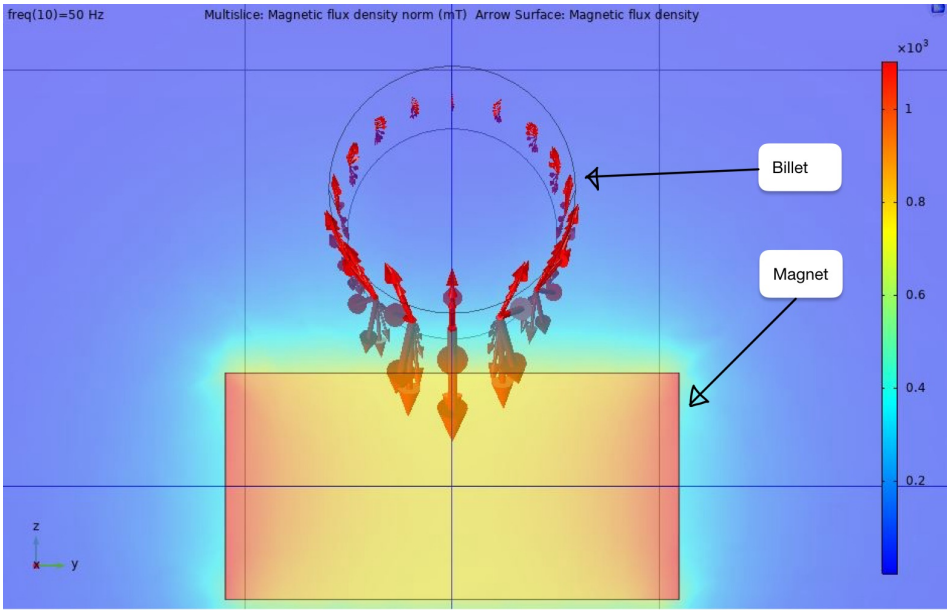

Figure 49: 3D model of the system showing the billet from the front.

In Figure 50 the magnet is rotating, the red arrows represent the magnetic flux density and the interaction with the billet. This model shows the distribution of the flux throughout the volume of the billet. Here, the contribution of magnetic flux is most evident in the x- and the z-directions.

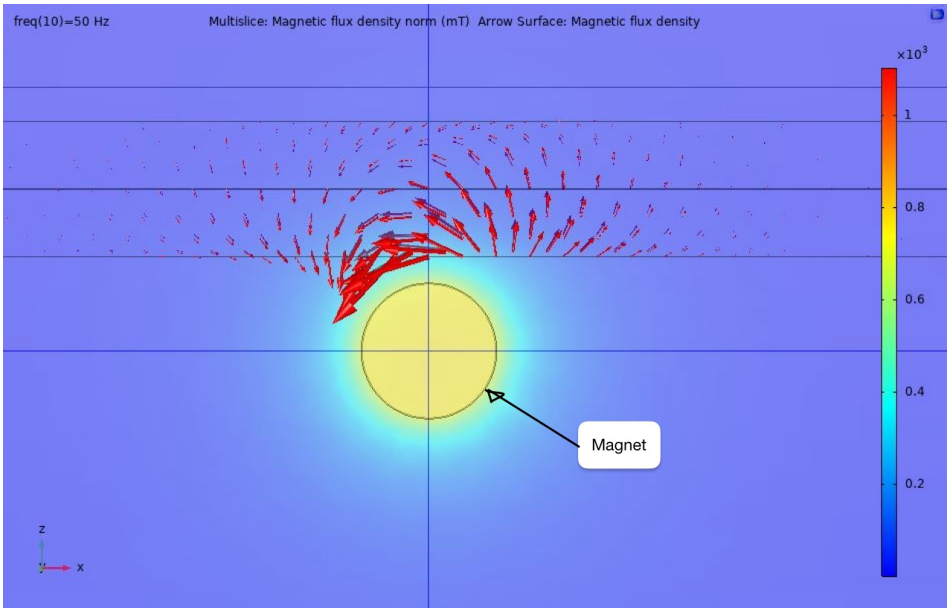

Figure 50: 3D model of the system from the side, showing the flux line distribution in the billet clearly.

In addition to the 3D-model views, there were some 2D plots that also show the development of the magnetic field through the billet. Seen from the front in Figure 51a and 51b. It is shown from the side in Figure 52a and 52b. The field lines are curved inward at higher RPM, reducing the interaction volume and focusing near the surface as predicted by the skin effect discussed in 2.3.5. These plots give a good indication of the actual development of the field, showing what was calculated by Equation 10 and displayed in Figure 42. The 2D plots of the penetration Figure 51b, and Figure 52b, generally agree with the calculated penetration in Figure 42.

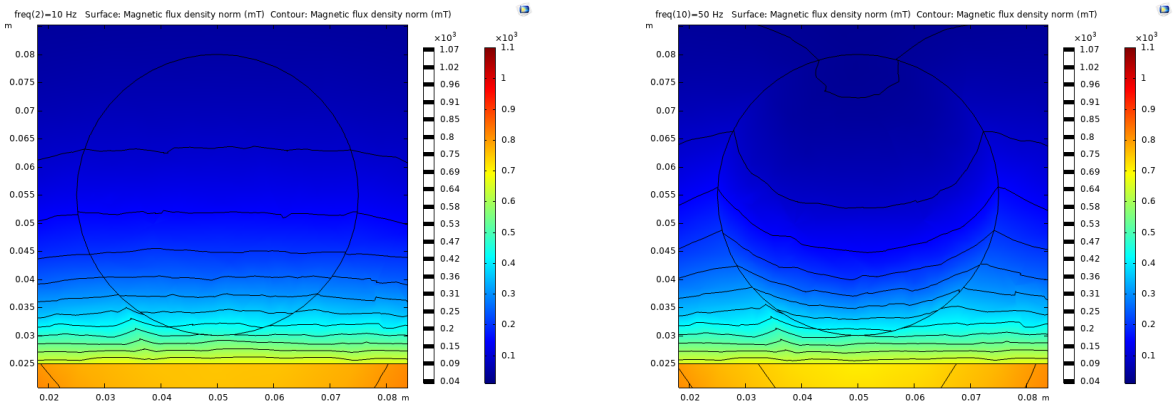

(a) 10Hz (b) 50Hz

Figure 51: The penetration of the magnetic field lines through the billet seen from the front of the billet.

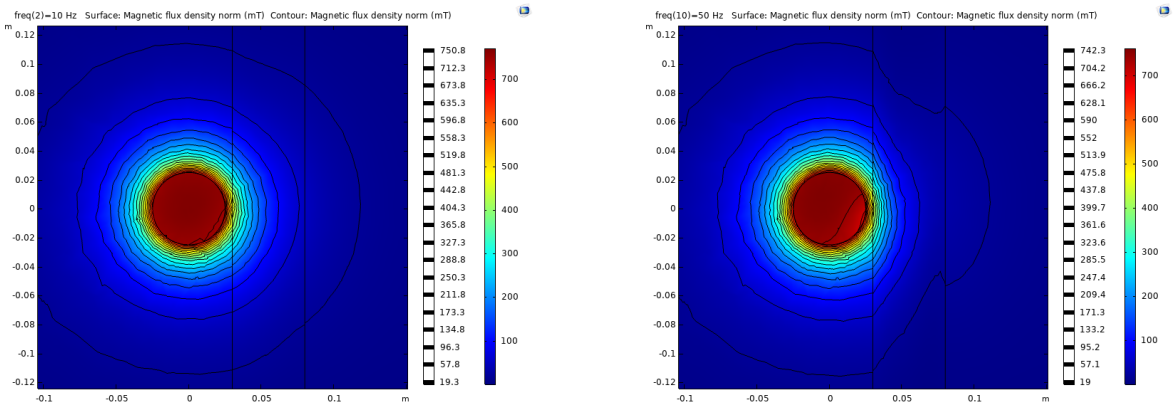

(a) 10Hz (b) 50Hz

Figure 52: The penetration of the magnetic field lines through the billet seen from the side.

Results from the FEM simulation, at 0.5cm, are shown in Table 11. From this, an increase of volumetric loss density, electromagnetic [W], by increasing frequency. This simulation generates 272W at 55Hz and maxes out with 485W at 100Hz. For the Lorentz force contribution, time average, x-component [N], the force increases, then flattens out at around 70Hz, at 27N. From the Lorentz force contribution, time average, and z-component [N], there is still an increase in force at 100Hz, reaching 40N.

Table 11: COMSOL Multiphysics® induction loss modelling simulation, 0.5cm above billet (6060).

Frequency [Hz]	Volumetric loss density, electromagnetic [W]	Lorentz force contribution, time average, x component [N]	Lorentz force contribution, time average, z component [N]
5	4.5321	-4.2749	0.46039
10	17.602	-8.3408	1.7850
15	37.804	-12.031	3.8215
20	63.266	-15.246	6.3665
25	92.098	-17.952	9.2141
30	122.69	-20.169	12.189
35	153.85	-21.947	15.160
40	184.77	-23.350	18.039
45	214.97	-24.443	20.775
50	244.19	-25.285	23.342
55	272.35	-25.925	25.733
60	299.43	-26.405	27.949
65	325.48	-26.760	29.999
70	350.57	-27.015	31.894
75	374.79	-27.192	33.648
80	398.22	-27.307	35.274
85	420.92	-27.373	36.782
90	442.98	-27.401	38.184
95	464.45	-27.397	39.491
100	485.39	-27.368	40.712

Furthermore, results from the FEM simulation, at 2.0cm, are shown in Table 12. Also, an increase of volumetric loss density, electromagnetic [W], by increasing frequency. This simulation generates 95W at 55Hz and maxes out with 162W at 100Hz. For the Lorentz force contribution, time average, x-component [N], the force increases, then flattens out at around 40Hz, at 6N. From the Lorentz force contribution, time average, and z-component [N], it seems possible to flatten out around 12N at 95Hz.

Table 12: COMSOL Multiphysics® induction loss modelling simulation, 2.0cm above billet (6060).

Frequency [Hz]	Volumetric loss density, electromagnetic [W]	Lorentz force contribution, time average, x component [N]	Lorentz force contribution, time average, z component [N]
5	1.6887	-1.2230	0.15661
10	6.5424	-2.3769	0.60546
15	13.996	-3.4071	1.2908
20	23.302	-4.2826	2.1390
25	33.718	-4.9955	3.0766
30	44.623	-5.555	4.0424
35	55.567	-5.9803	4.9922
40	66.262	-6.2939	5.8980
45	76.549	-6.5181	6.7447
50	86.358	-6.6722	7.5260
55	95.675	-6.7726	8.2416
60	104.52	-6.8323	8.8944
65	112.93	-6.8615	9.4890
70	120.94	-6.8678	10.031
75	128.6	-6.8573	10.525
80	135.94	-6.8345	10.977
85	143.01	-6.8027	11.391
90	149.84	-6.7644	11.771
95	156.45	-6.7217	12.122
100	162.87	-6.6757	12.446

Comparing the models with the experimental results there are generally good correlations with a few notable examples. First is the experimental heat loss. This does not correlate that well with the model results, especially for the experiment at 2.0cm above the billet where the average experimental value was 160.533W and the model result was 95.675W at 55Hz seen in Figure 46 and Table 11 respectively. Inconsistencies like this are expected but not at this magnitude. The cause may be linked to the temperature gradient as this is one of the main variables in Equation 14 which was used to calculate the experimental values. This could relate to the insulation of the billet or the position of the magnet, as this was not in the same position as seen in the model. This can be seen in Figure 48 for the position in the model, and on Figure 28 for the position in the experiment

Second is the Lorentz force contribution. From Table 11 the expected force contribution from the x-direction is 25.925N at 55Hz compared to the measured value of around 34N from Figure 40. The same discrepancy is true for the model values in Table 12. It was calculated that the force contribution in the x-direction is 6.7722N at 55Hz, while the measured value seen in Figure 40 is around 10N. The reason for this discrepancy is likely that the load cell measured contributions from both the x- and z-directions instead of only the x-axis as it is presented in the model. This could be the result of the z-contribution displacing the cross-sectional area of the billet, making it tilt slightly upwards thus adding a contribution from the z-direction to the load cell. Interestingly, Appendix E presents the modelling of induction loss at 1.0cm above the billet. Here, values correlate closer to the experimental trial at 2.0cm above the billet. Possible reasons for this could be as discussed above and in 4.1.

Comparing the heating effect from the experimental trial and the values from modelling at 0.5cm above the billet, there is a closer correlation. Where the effect from the experimental trial averaged around 300W, the model from Table 11 shows approximately 270W at 55Hz.

Comparing the experimental values for the decreasing force caused by the loss in magnetic magnitude Figure 42 and the FEM models of the penetration depth Figure 51, Figure 52 reveal that the model is very accurate in describing the behaviour of the magnetic field inside the billet. This can be seen when comparing the active interaction volume defined by both sources, which is around two penetration depths at 50 Hz.

4.4 Validation with liquid aluminium

Results from the validation test do not produce legitimate numbers on flow. However, this test highlights visual effects and ease of setup. Figure 53 shows liquid aluminium before the introduction of the rotating magnetic field. Figure 54 is liquid aluminium with a rotating magnetic field induced. Here, a clear disturbance and motion of the liquid were observed. This also proved to be the case while adjusting the angle and location of the liquid relative to the magnet.

Figure 53: Liquid aluminium before validation test.

Figure 54: Liquid aluminium during validation test.

The flow of liquid aluminium was greater than anticipated, hence the adjustment in speed from 53.26Hz to 37.28Hz. This made it easier to control the liquid so that spillage was avoided. Still, after the adjustment, the amount of movement was notable and more controllable. The movement is caused by MHD and is here a visually plausible concept.

5 Conclusion

In this section, the closing thoughts will be presented with a following section on the future work that is recommended to follow up on to study other interesting theories that were outside of the scope of this thesis or were unable to be completed within the time frame. After analyzing and discussing the results of the test rig the following conclusions were drawn.

The groundwork proves firstly that rotating dipole permanent magnets with inner magnetization of 1.45T are able to provide considerable thrust to aluminium billets of the 6xxx series. This already confirms that further studies of replacing electromagnets with permanent magnets for the pumping of liquid metal are viable.

When using rotating permanent magnets to move aluminium, the motor force is translated into the rotation of the magnet, while the magnet does the work and the motor experiences a load, equal to the sum of thrust, induced heat and friction losses. The billet will as a consequence experience heating, which for this application is a relatively effective side effect. At frequencies close to the range in the experiments, the heating is not sufficient to be a problem for any processes even after numerous trials the aluminium billet was possible to touch without protective gloves. Comparing this to using EMPs, where the heat is induced mainly in the copper coils used to create the EM by resistivity and only a fraction in the metal by induction. The losses in a PMP will probably be smaller as there is no heating occurring in the magnet itself, only in the billet.

The forces that have been measured are very promising for applications within liquid pumping. From the validation test alone as discussed in section 4.4 there is a noticeable disturbance of the aluminium surface. This confirms the possibility of using permanent magnets. Later during the trials proper data and more observations strongly suggest that the concept is feasible in practice, reaching force values of up to 37N depending on the alloy Figure 40. Based on the strong results from the tests on the solid aluminium and assuming the current density to be the governing controllable variable for the Lorentz forces, liquid aluminium should not yield very different force readings. As liquid aluminium has a lower conductivity one could expect better penetration depth with a weaker force distribution in the aluminium. This weaker force should still be sufficient for effective stirring seeing as the liquid aluminium would be more prone to deformation and movement than a solid billet of aluminium. The main issue of using a permanent magnet in practical applications would be the distance between the liquid and the magnet. However with a magnet of the same type, one could still expect stirring even at distances of 3.0cm between the magnet and the liquid. This is due to the electromagnetic waves still being able to penetrate aluminium even at longer ranges effectively.

The penetration depth of the magnetic field is one of the more important parameters to consider according to the experimental results Figure 44. Considering that the experimental data, Figure 42 was able to corroborate the validity of the model Figure 51, it will be easier to follow up on the work with eventual tweaks to the geometry of the billet itself to maximize the interaction volume.

Summarizing conclusions:

- Rotating dipole permanent magnets with 1.45T inner magnetization can provide significant thrust to 6xxx series aluminium billets, indicating a potential for replacing electromagnets in liquid metal pumping.
- Experimental results show promising forces up to 37N, suggesting the feasibility of using PMPs for liquid aluminium pumping. Liquid aluminium, with its lower conductivity, should still experience sufficient stirring forces at practical distances.
- The penetration depth of the magnetic field is crucial, with experimental data validating the model and indicating the potential for optimizing billet geometry to enhance interaction volume.

6 Future Work

For future work, the main focus should be to initiate more liquid metal trials. Because of the short time frame of the thesis, the actual liquid metal loop was not ready for experiments, hence there was only one liquid metal trial. For other experiments it would be interesting to look at how different shaped billets and canals are affected by the magnetic field and if this would give results worth pursuing. The reason for this has to do with the penetration of the magnetic field through the billet and the forces that would result from this. This could also lead to a more thorough study of how the penetration depth and current densities will affect the Lorentz force distribution.

It is also worth noting that while the thesis did touch upon many concepts related to electromagnetism, there were no trails using electromagnetic coils. This is a topic that could be expanded upon, especially when comparing the advantages and disadvantages of permanent over electromagnets.

References

[1] Neodymium magnet manufacturing: Techniques and processes, 2023. accessed 15.05.24 at https://www.greatmagtech.com/info/neodymium-magnet-manufacturing-techniques-and-83821571.html.

[2] T. Beinerts A. Bojarevics. Experiments on liquid metal flow induced by a rotating magnetic dipole. *Magnetohydrodynamics*, Volume 46:pages 333–338, 2010.

[3] The Aluminum Association. International alloy designations and chemical composition limits for wrought aluminum and wrought aluminum alloys. pages 1–31, 2018.

[4] Marachio C. The production of ndfeb magnets, 2024. accessed 15.05.24 at https://www.stanfordmagnets.com/the-production-of-ndfeb-magnets.html.

[5] Steven W. Ellingson. *Electromagnetics, Vol. 1. Blacksburg*. VA: Virginia Tech Publishing, 2018.

[6] Steven W. Ellingson. *Electromagnetics, Vol. 2. Blacksburg*. VA: Virginia Tech Publishing, 2020.

[7] Robert Fritzsch. *Electromagnetically Enhanced Priming of Ceramic Foam Filters*. PhD thesis, Norwegian University of Science and Technology Faculty of Natural Sciences and Technology Department of Materials Science and Engineering, 2016.

[8] F.W.Bell. The hall effect gaussmeter. https://fwbell.com/wp-content/uploads/2019/04/Hall_Effect_Gauss.pdf, 2019. Accessed on 23.04.2024.

[9] E. Golbraikh P. Frick A. Kapusta B. Mikhailovich I. Kolesnichenko, A. Pavlinov. The study of turbulence in mhd flow generated by rotating and traveling magnetic fields. *Exp Fluids*, 88:1–11, 2014.

[10] Roger Lumley. *Fundamentals of aluminium metallurgy: production, processing and applications*. Elsevier, 2010.

[11] Kirk T. McDonald. Methods of calculating forces on rigid, linear magnetic media. pages 1–17, 2002.

[12] U.S. Department of Energy. Doe fundamentals handbook electrical science. 4:1–4, 1992.

[13] United States. National Bureau of Standards. *Copper wire tables*. Washington Government Printing Office, 1914.

[14] P Olafsson, R Sandstrom, and Å Karlsson. Comparison of experimental, calculated and observed values for electrical and thermal conductivity of aluminium alloys. *Journal of materials science*, 32:4383–4390, 1997.

[15] Enrique J. Dede: Member IEEE José M. Burdío: Senior Member IEEE Oscar Lucía: Member IEEE, Pascal Maussion: Member IEEE. Induction heating technology and its applications: Past developments, current technology, and future challenges. *IEEE TRANSACTIONS ON INDUSTRIAL ELECTRONICS*, 61, No. 5, 2014.

[16] G. Neuer R. Brandt. Electrical resistivity and thermal conductivity of pure aluminum and aluminum alloys up to and above the melting temperature. *International Journal of Thermophysiscs*, 28:1429–1445, 2007.

[17] Grayson. J R. Fritzsch. *Electromagnetic Transfer and Circulation (ETAC) of Molten Aluminum Metal and Its Alloys*. Springer International Publishing, 2019.

[18] Mark E. Schlesinger. *Aluminium Recycling Second Edition*. Taylor Francis Group, 2010.

[19] Christoph Schmitz. *Handbook of aluminium recycling*. Vulkan-Verlag GmbH, 2006.

[20] I. Bucenieks Y. Gelfgat I. Kaldre T. Beinerts, A. Bojarevics. Use of permanent magnets in electromagnetic facilities for the treatment of aluminum alloys. *Metallurgical and Material Transactions B*, 47B, 2016.

[21] Richard J. D. Tilley. *Understanding Solids*. John Wiley Sons, 2004.

[22] Iowa State University. Magnetic permeability. https://www.nde-ed.org/Physics/Materials/Physical_Chemical/Permeability.xhtml, 2024. Accessed on 29.04.2024.

[23] A. Bojarevičs M. Mīlgrāvis Ģ. Zāģeris V. Geža, A. Gaile and S. Pavlovs. Electromagnetically generated waves on free surface of liquid metal for refinement processes. *Heating by Electromagnetic Sources*, 19:264, 2019.

[24] David G. Rethwisch William D. Callister Jr. *Materials Science and Engineering*. John Wiley & Sons (Asia) Pte Ltd, 2015.

Appendix

A Risk assessment

Enhet/Institutt:	Institutt for materialteknologi
Ansvarlig linjeleder (navn):	Ida Westermann
Ansvarlig for aktiviteten som risikovurderes (navn):	Robert Fritzsch
Deltakere (navn):	Magnus Breimo, Odin Vassbotn Breivik

Beskrivelse av den aktuelle aktiviteten, området mv.:

Aktiviteten går utpå å bygge et eksperimentelt utstyr som skal brukes til å utføre eksperiment på flytende aluminium med kraftige permanente og elektromagnetiske magneter

Aktivitet/arbeidsoppgave	Mulig uønsket hendelse	Eksisterende risikoreduserende tiltak	Vurdering av sannsynlighet (S) (1-5)	Vurdering av konsekvens (K) Vurder en konsevenskategori om gangen. Menneske skal alltid vurderes. Menneske (1-5)	Ytre miljø (1-5)	Økk/materiell (1-5)	Omdømme (1-5)	Risikoverdi (S x K)	Forslag til forebyggende og/eller korrigerende tiltak Prioriter tiltak som kan forhindre at hendelsen inntreffer (sannsynlighetsreduserende tiltak) foran skjerpet beredskap (konsekvensreduserende tiltak)	Restrisiko etter tiltak (S x K)
Bygging av utstyr	Skade rygg	Vernesko, Vernehansker	1	2			1	2	Bruke hjelpeutstyr	1
	Klemskader		2	2			1	4		4
	Støt		1	2			1	2		2
Håndtering av metall loop	Skade på magnetisk materiell		3			4	2	0		0
	Brannskader	Vernehansker	2	2				4	Unngå å berøre utstyret under drift	1
	Støt		1	2				2		2
	Fosfingassutvikling		2	4				8	Avtrekk	4
Flytte flytende aluminium	Søl på menneske	Flammehemmende klær, vernesko	1	3				3	Ansiktsskjold	2
	Søl på gulv		3			2		0		0
Kutte aluminium	Kutteskader	Vernehansker	1	3				3		3
	Sette seg fast i båndsag		2	3				6	Unngå lange ermer og andre ting som kan sette seg fast i sag	3
Drille aluminium	Kutteskader	Vernehansker	1	3				3		3
	Sette seg fast i roterende deler		2	3				6	Unngå lange ermer og andre ting som kan sette seg fast i sag	3

B Gear change calculations

Calculating gear change

From Parker Ac 10 series inverter specifications:

$28 \frac{RPM}{Hz}$ input frequency to magnet RPM

Gear diameters: [mm]

1: 130,8

2: 109,8

3: 84

4: 57,4

5: 34

1-4 at 50 input Hz:

$(50\,Hz \cdot 28 \frac{RPM}{Hz}) \cdot \frac{130,8\,mm}{57,4\,mm}$

$= 3190,24\ RPM$

To true Hz:

$\frac{3190,24\ RPM}{60_s} = 53,17\ Hz$

4-1 at 50 input Hz:

$(50Hz \cdot 28 \frac{RPM}{Hz}) \cdot \frac{57,4\,mm}{130,8\,mm}$

$= 614,37\ RPM$

To true Hz:

$\frac{614,37}{60_s} = 10,24\ Hz$

C Thrust graphs

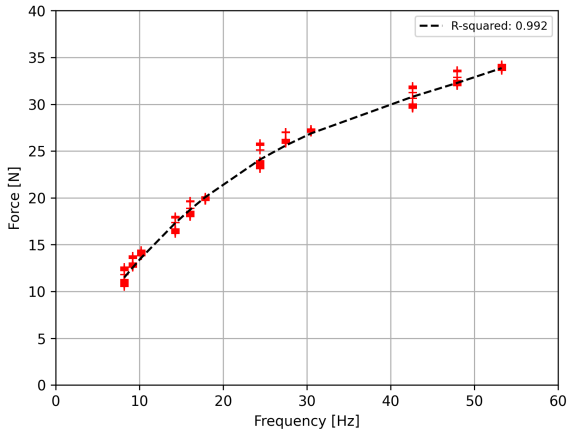

(a) Force readings at 0.5 cm away from the billet

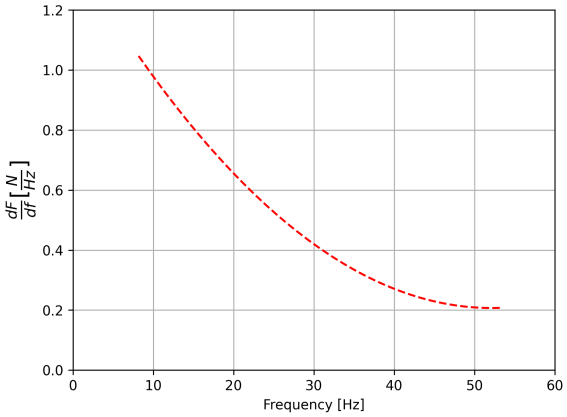

(b) Derivative of the force readings 0.5 cm away from the billet

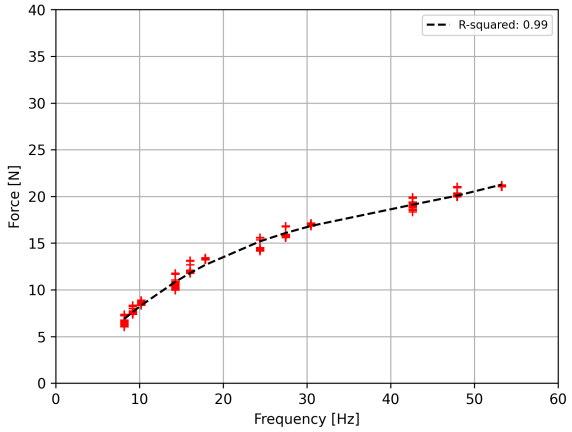

(a) Force readings 1.0 cm away from the billet

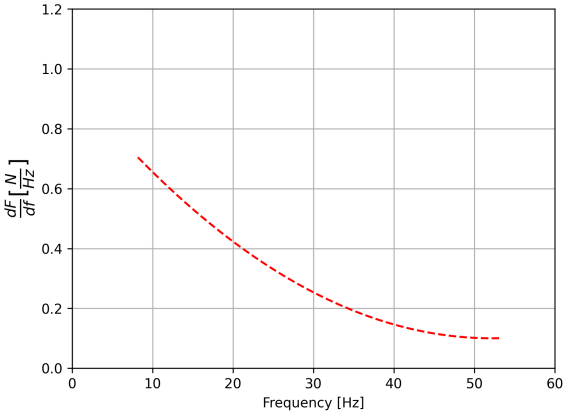

(b) Derivative of the force readings 1.0 cm away from the billet

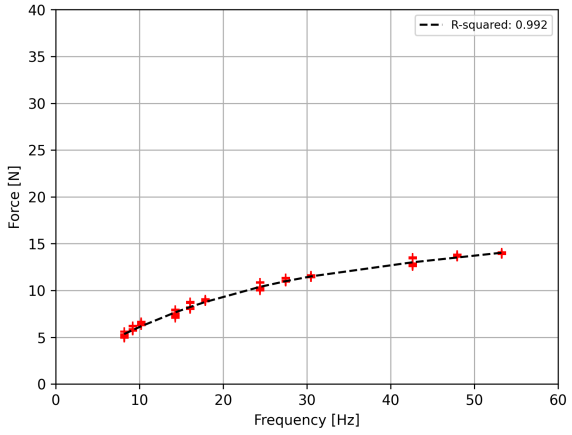

(a) Force readings 1.5 cm away from the billet

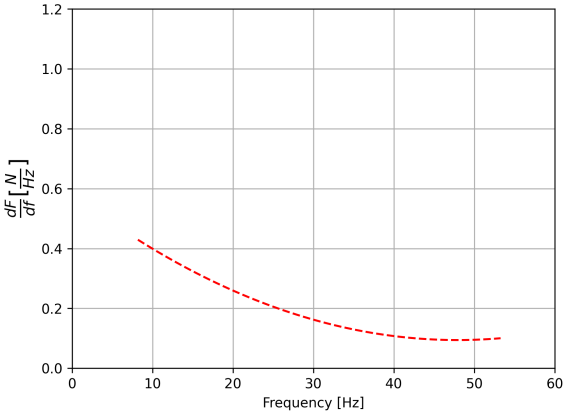

(b) Derivative of force readings 1.5 cm away from the billet

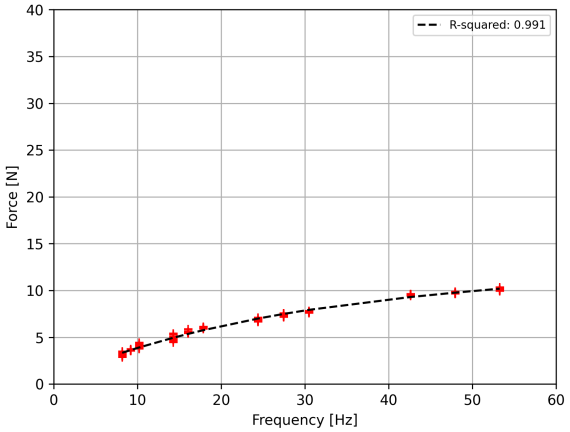

(a) Force readings 2.0 cm away from the billet

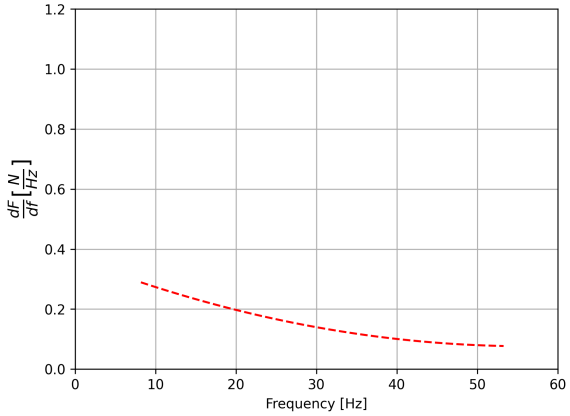

(b) Derivative of force readings 2.0 cm away from the billet

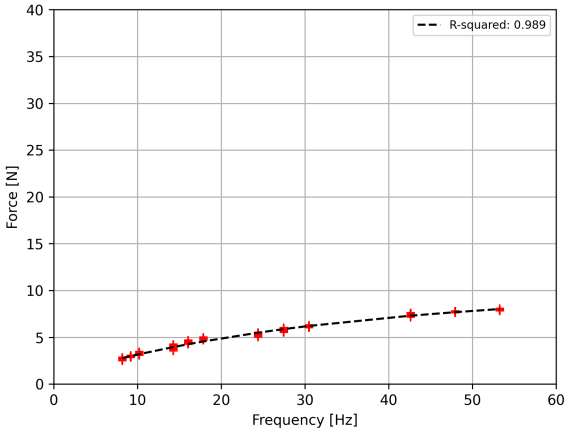

(a) Force readings 2.5 cm away from the billet

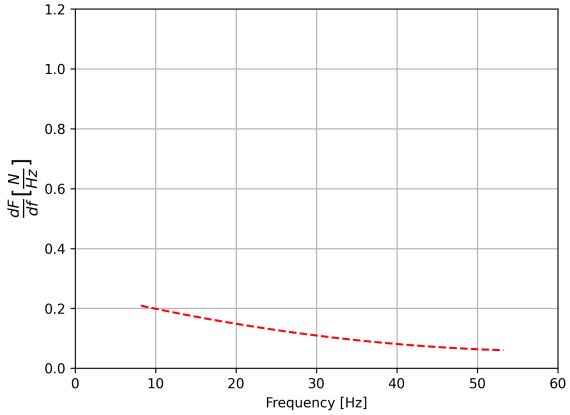

(b) Derivative of force readings 2.5 cm away from the billet

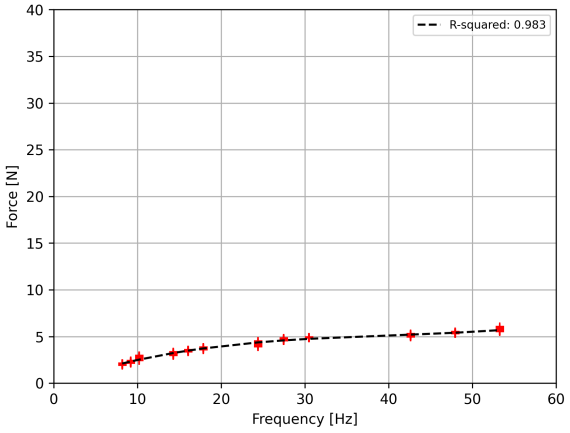

(a) Force readings 3.0 cm away from the billet

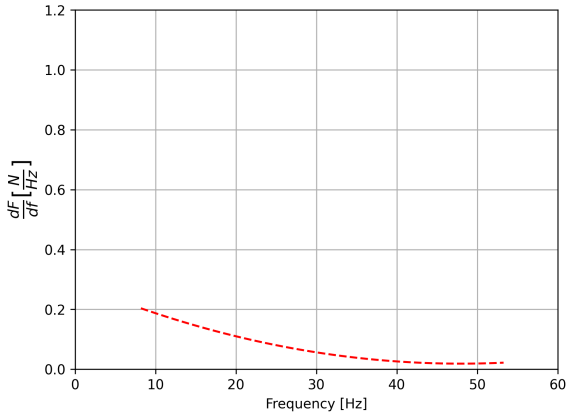

(b) Derivative of force readings 3.0 cm away from the billet

D Derivation of penetration depth

Skin effect

tirsdag 7. mai 2024 12:59

$e^{-\alpha l}$

$$\boxed{\delta_s = \frac{1}{\alpha}} \quad (3.159)$$

Skin depth δ_s is the distance over which the magnitude of the electric or magnetic field is reduced by a factor of $1/e \cong 0.368$.

$$e^{-\alpha\delta_s} = e^{-1} \cong 0.368 \quad (3.158)$$

$e^{-\alpha l}$

Defining attenuation in terms of Skin depth (δ_s).

$e^{-\alpha \delta_s} = e^{-1}$

From this equation, the following must be true:

$\delta_s = \frac{1}{\alpha}$

Defining an equation for loss in electromagnetic field strength as a function of distance

$e^{-\alpha \delta_s} = e^{-1}$

$\Rightarrow e^{-\alpha(\frac{l}{\delta_s} \cdot \delta_s)}$

Defining a fraction of the skin depth as a function of distance into the billet.

$\Rightarrow e^{-\alpha\left(\frac{l}{\delta_s} \cdot \frac{1}{\alpha}\right)}$

$\Rightarrow e^{-\frac{l}{\delta_s}}$

$\Rightarrow \frac{1}{e^{\frac{l}{\delta_s}}}$

Skin effect Page 1

E Modelling from COMSOL Multiphysics® 5.5

Table 13: COMSOL Multiphysics® induction loss modelling simulation, 1.0cm above billet (6060)

Frequency [Hz]	Volumetric loss density, electromagnetic [W]	Lorentz force contribution, time average, x component [N]	Lorentz force contribution, time average, z component [N]
5	3.1964	-2.7321	0.31536
10	12.402	-5.3225	1.2216
15	26.592	-7.6586	2.6111
20	44.411	-9.6742	4.3407
25	64.492	-11.349	6.2664
30	85.686	-12.700	8.2667
35	107.14	-13.762	10.252
40	128.31	-14.580	12.163
45	148.85	-15.198	13.967
50	168.61	-15.657	15.649
55	187.55	-15.991	17.204
60	205.67	-16.227	18.636
65	223.02	-16.386	19.953
70	239.66	-16.488	21.163
75	255.66	-16.544	22.276
80	271.08	-16.565	23.301
85	285.99	-16.560	24.248
90	300.44	-16.533	25.124
95	314.48	-16.492	25.937
100	328.25	-16.437	26.692

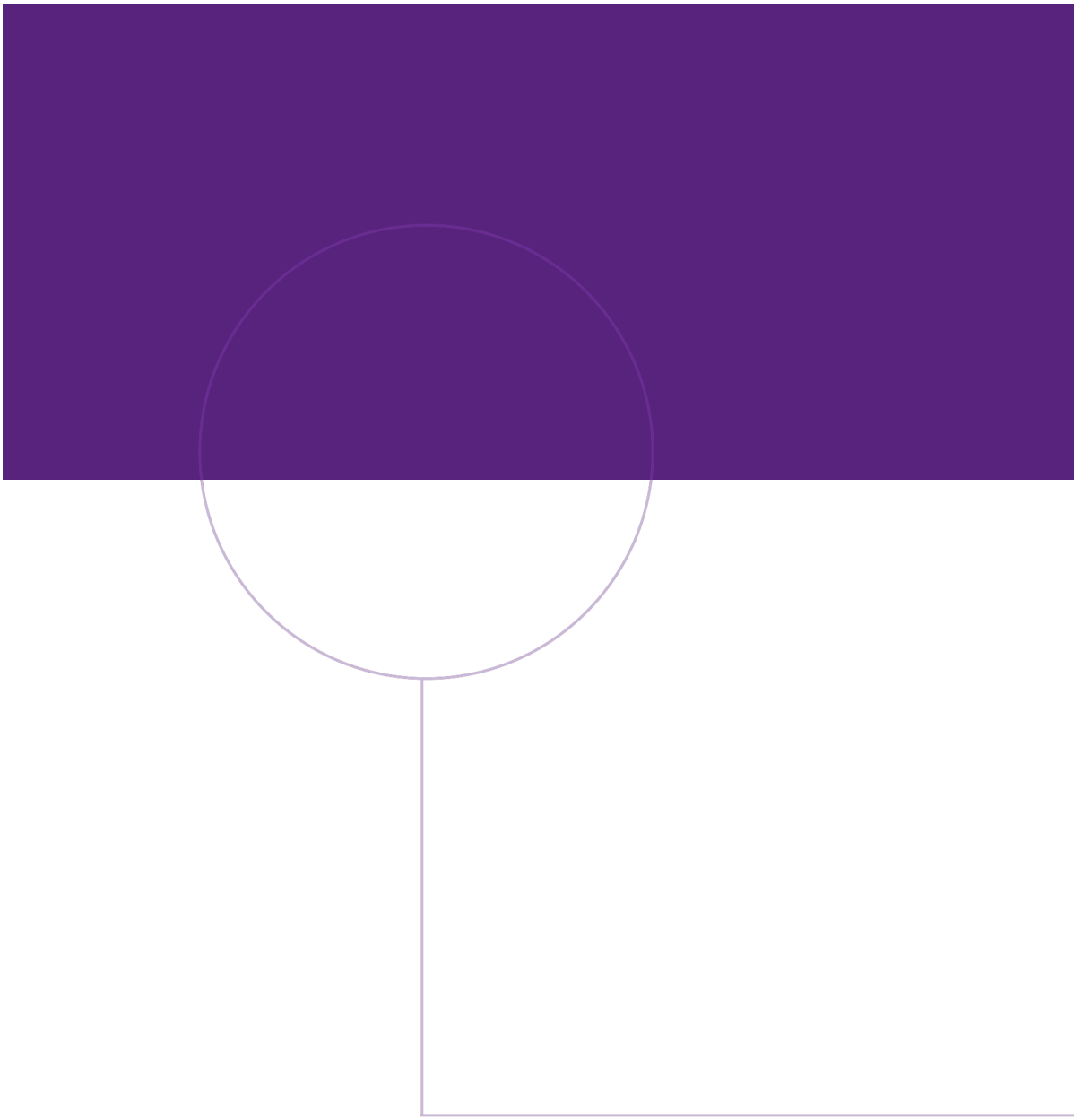

NTNU
Norwegian University of
Science and Technology

Pyrotek